Applied Catalysis B: Environmental 224 (2018) 983–999

Contents lists available at ScienceDirect

Applied Catalysis B: Environmental

journal homepage: www.elsevier.com/locate/apcatb

Review

First-principle calculation study of tri-*s*-triazine-based g-C_3N_4: A review

Bicheng Zhu[a], Liuyang Zhang[a], Bei Cheng[a], Jiaguo Yu[a,b,*]

[a] State Key Laboratory of Advanced Technology for Materials Synthesis and Processing, Wuhan University of Technology, Wuhan 430070, PR China
[b] Department of Physics, Faculty of Science, King Abdulaziz University, Jeddah 21589, Saudi Arabia

ARTICLE INFO

Keywords:
g-C_3N_4
Density functional theory
Electronic property
Photocatalysis

ABSTRACT

Graphitic carbon nitride (g-C_3N_4) is an attractive photocatalyst which has appealing visible light absorption, outstanding layered porous structure, high stability and nontoxicity. Many experimental methods have been developed to modify the pristine g-C_3N_4 and enhanced photocatalytic activities have been witnessed. First-principle calculation based on density functional theory is an effective approach to investigate the structural, electronic, optical and thermodynamic properties of molecules and crystals, which provides important information to elucidate the improved photocatalytic activity of modified g-C_3N_4 at atomic or unit-cell levels, or even further, to predict the property and photocatalytic activity of experimentally un-synthesized g-C_3N_4-based photocatalysts. This review is dedicated to this important material, i.e. tri-*s*-triazine-based g-C_3N_4 and summarized a panorama of the major advances in the first-principle investigation. The existing challenges and future directions at the forefront of this emerging research hotpot have also been discussed.

1. Introduction

In 1989, Liu and Cohen constructed a carbon nitride (C_3N_4) structure by substituting Si in β-Si_3N_4 with C and named it β-C_3N_4 [1]. Based on *ab initio* calculation, they predicted that this newly-created structure formed a hard material with bulk modulus comparable to or even greater than diamond. Four years later in 1993, the quasiparticle band gap of β-C_3N_4 was calculated to be 6.4 ± 0.5 eV by Corkill and Cohen [2]. Not long afterward, two more structures of C_3N_4 other than hexagonal β-C_3N_4 were assumed by Liu and Wentzcovitch: zinc-blende-like cubic C_3N_4 and layered graphite-like rhombohedral C_3N_4 [3]. Till 1996, Teter and Hemley proposed five structures of C_3N_4, including α-C_3N_4, β-C_3N_4, cubic-C_3N_4, pseudocubic-C_3N_4 and graphitic-C_3N_4 (g-C_3N_4) [4]. First-principle calculation showed that the total energy of g-C_3N_4 was the lowest. Thereafter, various forms of g-C_3N_4 were investigated, including *s*-triazine-based hexagonal structure, *s*-triazine-based orthorhombic structure and tri-*s*-triazine (heptazine)-based structure (Fig. 1) [5–8]. Based on density functional theory (DFT) calculations, Kroke et al. found that the tri-*s*-triazine-based structure was the most stable structure among all the allotropes of g-C_3N_4 [9]. Henceforth, this structure is recognized as the building blocks for g-C_3N_4 in later studies.

Since the pioneering report of photocatalytic H_2 production on tri-*s*-triazine-based g-C_3N_4 [10], various kinds of photocatalytic studies of g-C_3N_4 sprung up swiftly; to name a few, degradation of pollutants (NO, CO, UO_2^{2+}, phenol and organic dye) [11–18], splitting of water [19–21] and reduction of CO_2 [22–24]. Nevertheless, it was gradually realized that the photocatalytic activity of pristine g-C_3N_4 was unsatisfied due to its limited visible light absorption, poor textural property and serious recombination of photogenerated electron–hole pairs [25,26]. Many modifications have been adopted to improve the photocatalytic activity of g-C_3N_4, such as introduction of foreign element [27–29], construction of composite [30–35], and design of novel morphology and structure [36,37]. The enhanced activities were usually experimentally explained by the judiciously engineering properties consisting of optical, textural and photoelectrochemical property.

Although the experimental study on g-C_3N_4 has become the mainstream direction and it expanded exponentially, first-principle investigation based on DFT calculation has never stopped. Over time, computational research gradually turns its focus to the photocatalysis-related properties of pristine g-C_3N_4 and modified g-C_3N_4 (g-C_3N_4 with various unit-cell structures, impurity-doped g-C_3N_4 and g-C_3N_4-based composites). These computational studies aim to elucidate the improved photocatalytic activity of modified g-C_3N_4 microscopically, or more forward-looking, to predict the property and photocatalytic activity of a modified g-C_3N_4 which has not been synthesized experimentally.

Herein, the major advances in the first-principle investigation on tri-*s*-triazine-based g-C_3N_4 have been summarized for the first time. The whole manuscript comprises four parts: (1) basic properties of g-C_3N_4, (2) modifications of g-C_3N_4, (3) photocatalytic reaction on g-C_3N_4 and (4) summary and outlook. It should be noted that this manuscript emphasizes the research approach and computational results of the first-principle investigation on tri-*s*-triazine-based g-C_3N_4; while the

* Corresponding author at: State Key Laboratory of Advanced Technology for Materials Synthesis and Processing, Wuhan University of Technology, Wuhan 430070, PR China.
E-mail address: jiaguoyu@yahoo.com (J. Yu).

https://doi.org/10.1016/j.apcatb.2017.11.025
Received 29 September 2017; Received in revised form 7 November 2017; Accepted 10 November 2017
Available online 11 November 2017
0926-3373/

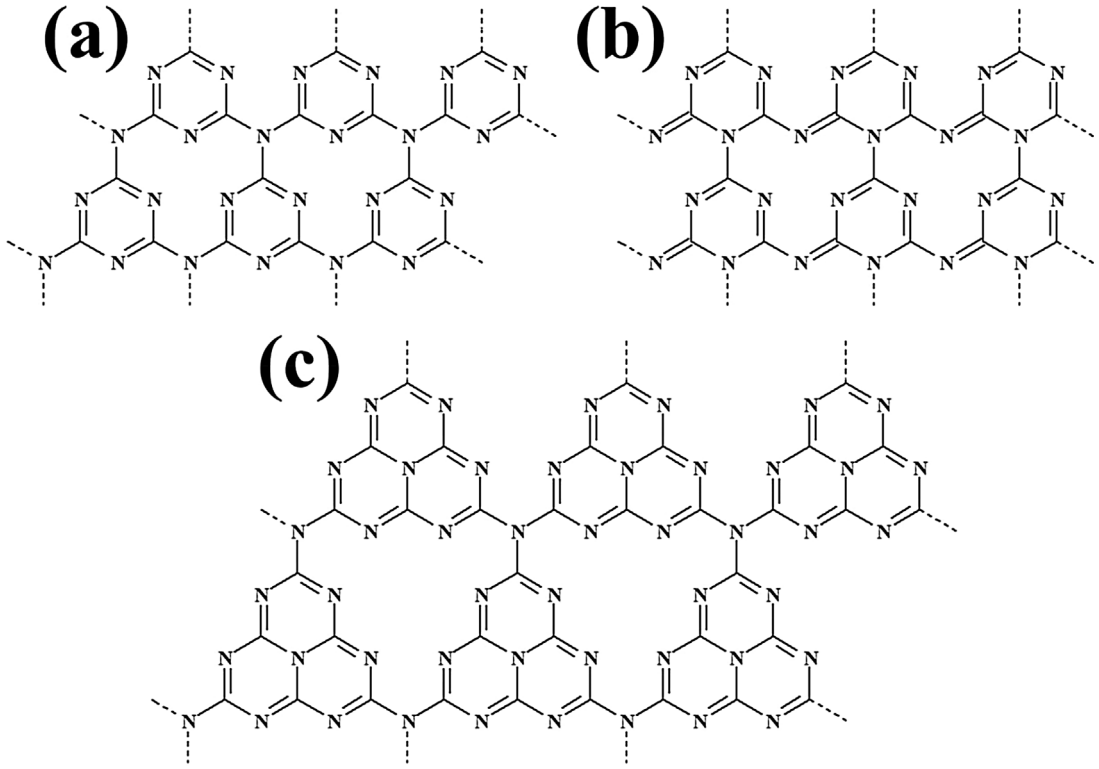

Fig. 1. Structural formulas of g-C_3N_4: (a) *s*-triazine-based hexagonal structure; (b) *s*-triazine-based orthorhombic structure; (c) tri-*s*-triazine-based structure.

computational details (adopted software and computational parameters) are not involved. It is anticipated that an overview picture of the recent development can be clearly stated in this review.

2. Basic properties of tri-*s*-triazine-based g-C_3N_4

2.1. Geometric structure

The unit cell of tri-*s*-triazine-based g-C_3N_4 is a layered structure with interlayer distance (d) of 3.19 Å (Fig. 2a) [38]. In each layer, repeated tri-*s*-triazine units are connected by nitrogen atoms (Fig. 2b). The lattice distance a is 7.14 Å [39]. Sixfold cavity is formed by encirclement of three adjacent heptazine units. There are three nonequivalent nitrogen atoms and two nonequivalent carbon atoms labelled as N1, N2, N3, C1 and C2, respectively. The N2 atom is two-coordinated and the rest are three-coordinated. The bond lengths of N1−C1, C1−N2, N2−C2 and C2−N3 bonds are 1.47 Å, 1.34 Å, 1.33 Å and 1.39 Å, respectively [40]. The bulk g-C_3N_4 is constructed by the "AB-stacking" of numerous layers. The interaction energy between neighboring layers is 0.036 eV $Å^{-2}$, corresponding to a van der Waals force caused by the weak π–π interaction between layers [41,42].

2.2. Band structure

It is well known that the generalized gradient approximation with the Perdew–Burke–Ernzerhof (GGA-PBE) functional usually underestimates the energy band gap (E_g) of a semiconductor. As for monolayer g-C_3N_4, the E_g calculated by GGA-PBE functional is 1.2 eV (Fig. 3a), which is 1.5 eV smaller than the experimental value (2.7 eV) [43,44]. By contrast, the HSE06 functional predicts more accurately: an exact E_g of 2.7 eV is achieved (Fig. 3b). In either case, g-C_3N_4 shows an indirect band gap with valance band maximum (VBM) and conduction band minimum (CBM) lying at different K points in the Brillouin zone.

2.3. Density of states and molecular orbitals

Fig. 4 shows the total density of states (TDOS), partial density of states (PDOS), highest occupied molecular orbital (HOMO) and lowest unoccupied molecular orbital (LUMO) of monolayer g-C_3N_4. The aforementioned information aims to attribute the energy band to specific atoms and disclose the favorable reduction and oxidation sites. It is found that the valence band (VB) edge is mainly composed of N2 atoms, and the conduction band (CB) edge mainly consists of C1, C2, N2 and N3 atoms (Fig. 4a). When specialized to atomic orbital, the VB edge is occupied by the N 2p orbital, and the CB edge is occupied by the C 2p and N 2p orbital [45]. This constitution is ascribed to the fact that N is more electronegative than C. It is a common rule for many photocatalysts (such as TiO_2, ZnO, ZnS, CdS and $Zn_{0.5}Cd_{0.5}S$) that the VB edge is composed of the element whose electronegativity is relatively higher [46–50]. The molecule orbitals further validate the DOS results. To be explicit, the HOMO covers all N2 atoms (Fig. 4b), and the LUMO is distributed on C1, C2, N2 and N3 atoms (Fig. 4c) [40]. As a result, the N2 atoms act as both oxidation and reduction sites, and the C1, C2 and N3 atoms are reduction sites in photocatalytic process. The bridging N (N1) atoms do not participate in HOMO or LUMO, and they contribute little to the CB and VB edges, suggesting that the electrons will not be generated on or be excited to N1 atoms, and the transfer of electrons from one heptazine unit to another unit through N1 atoms is suppressed. Hence, the photogenerated electrons are localized in each heptazine unit, resulting in high recombination rate of electron–hole pairs and poor photocatalytic activity of pristine g-C_3N_4 [42,51].

2.4. Work function

The work function (Φ) is defined as the minimum energy needed for an electron escaping from the Fermi energy level to the vacuum [52]. It is calculated using $\Phi = E_{vac} - E_f$, where E_{vac} and E_f are the vacuum energy and Fermi energy, respectively [53,54]. It should be noted here that the E_{vac} obtained by DFT calculation is not 0. The calculated Φ of a bulk and a monolayer g-C_3N_4 is 4.42 eV [55] and 4.66 eV [56], respectively. With

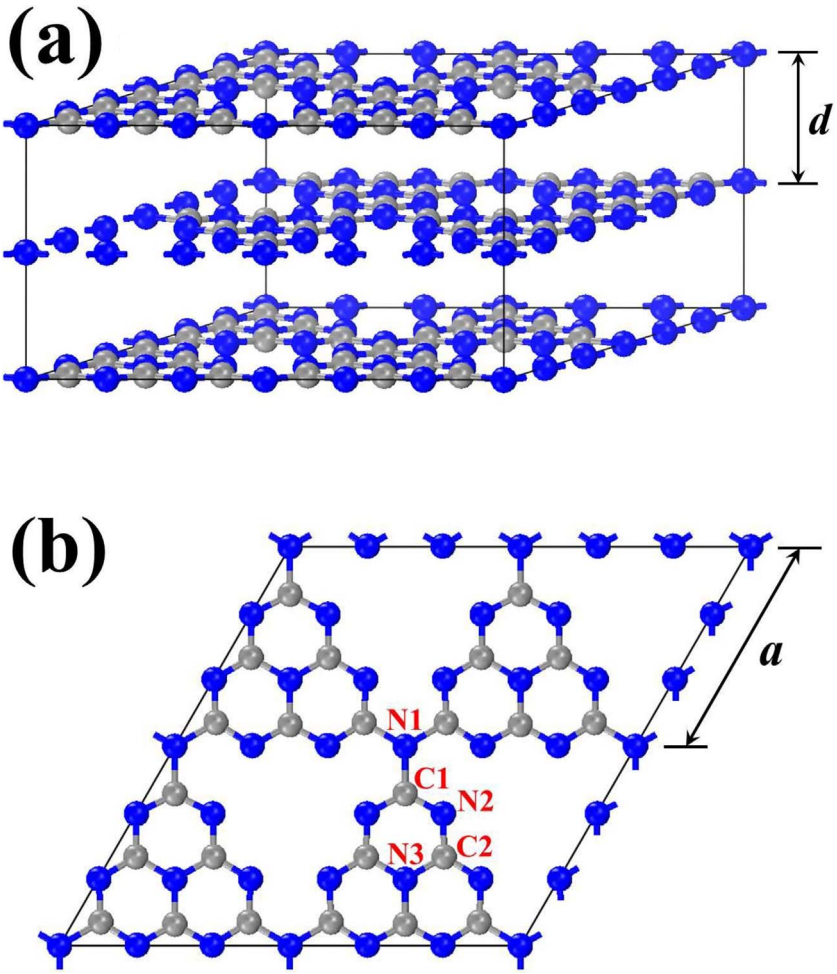

Fig. 2. Geometric structures of (a) bulk g-C_3N_4 and (b) single layer g-C_3N_4. The gray and blue balls are carbon and nitrogen atoms, respectively. (For interpretation of the references to colour in this figure legend, the reader is referred to the web version of this article.)

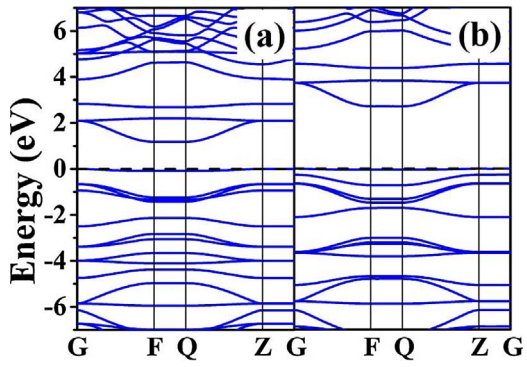

Fig. 3. Band structure of monolayer g-C_3N_4 calculated by (a) GGA-PBE and (b) HSE06 functional. The dashed line is the Fermi energy.

respect to photocatalytic mechanism, work function is commonly used to evaluate the Fermi energy. Experimentally, the CB and VB potentials are usually measured with normal hydrogen electrode (NHE) as reference. The absolute vacuum scale (AVS) is another reference. The relationship between NHE and AVS is $E_{NHE} = -E_{AVS} - E^e$, where E^e is the energy of the free electron on the hydrogen scale (*ca.* 4.5 eV) [57–59]. In the absolute vacuum scale, E_{vac} is taken as 0, and therefore Fermi energy is just the negative value of work function. In other words, a larger work function generally corresponds to a lower Fermi energy. When material A and material B are composited, their work functions can be calculated, and then their Fermi energies *versus* AVS are obtained and compared. Eventually, the transfer of electrons between A and B is determined according to the relative location of their Fermi energies.

2.5. Optical absorption

The optical absorption property is reflected by the curve of absorption coefficient (*I*) *versus* photon energy or wavelength. The absorption coefficient is defined as $I = \sqrt{2}\varpi[\sqrt{\varepsilon_1(\varpi)^2 + \varepsilon_2(\varpi)^2} - \varepsilon_1(\varpi)]^{1/2}$, where ϖ is photo frequency, ε_1 (ϖ) and ε_2 (ϖ) are the real and imaginary parts of dielectric function, respectively [60,61]. The optical absorption curve of monolayer g-C_3N_4 in Fig. 5 shows that g-C_3N_4 is responsive to visible light and the absorption edge is about 465 nm [62], in line with the experimental value of 460 nm [63,64].

2.6. Effect of pressure on the basic properties of g-C_3N_4

To deepen the understanding of the essential characteristic of g-C_3N_4, Ruan et al. investigated the effect of pressure on the basic properties of g-C_3N_4 [65]. They reported that as the pressure increased from 0 to 40 GPa, the lattice constant, volume of unit cell and band gap gradually decreased; on the contrary, the density of unit cell and optical absorption gradually increased. Interestingly, the relationship between the band gap (E_g, eV) of g-C_3N_4 and pressure (p, GPa) can be roughly expressed by a linear equation: $E_g = 2.7098–0.0241p$ (Fig. 6a). In addition, the thermodynamic properties of g-C_3N_4 at different pressures were also examined. As observed in Fig. 6b–d, all the thermodynamic parameters increased with temperature. Moreover, the influence of pressure on the vibrational internal energy weakened with increasing temperature; while the influence of pressure on the entropy strengthened. The heat capacity leveled off at 195 J mol^{-1} K^{-1} when temperature was higher than 1200 K.

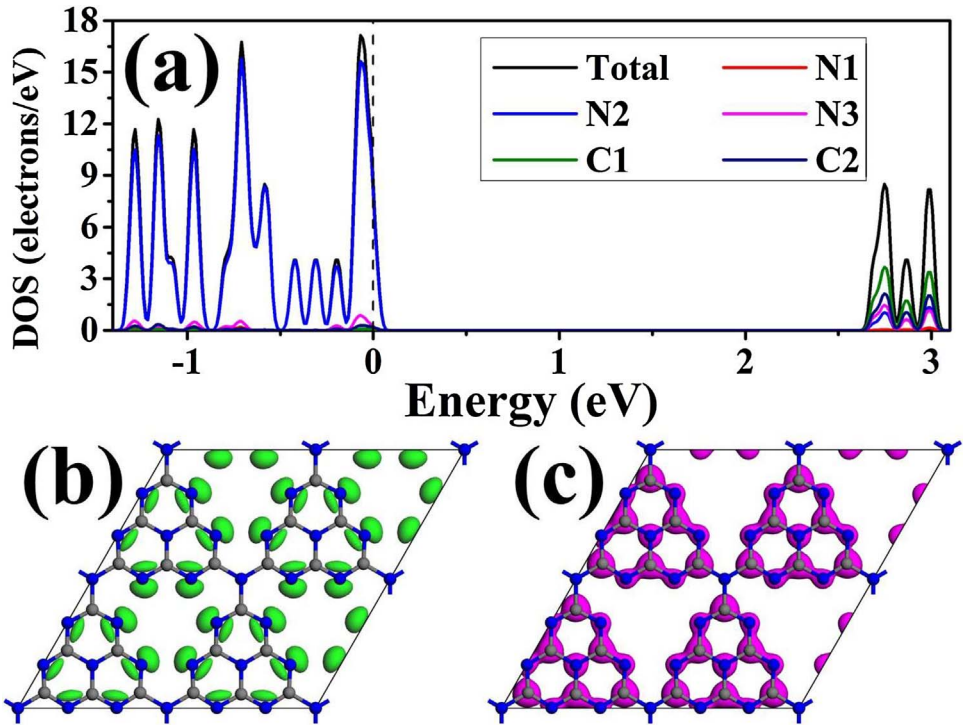

Fig. 4. (a) TDOS, PDOS, (b) HOMO and (c) LUMO of monolayer g-C_3N_4. The dashed line in (a) is the Fermi energy. Reprinted with permission from Ref. [40]. Copyright 2017 Elsevier.

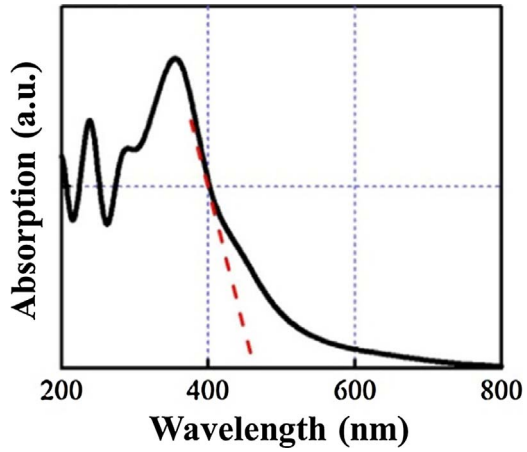

Fig. 5. Optical absorption curve of monolayer g-C_3N_4. Reprinted with permission from Ref. [62]. Copyright 2017 Elsevier.

3. Modifications of tri-*s*-triazine-based g-C_3N_4

3.1. Morphology engineering

The morphology of a photocatalyst plays a vital part in the photocatalytic activity, since it usually affects the specific surface area, pore structure, active site, light harvesting and scattering, as well as transfer mode of reactant and charge carrier. Generally, g-C_3N_4 synthesized by facile calcination of precursors (melamine, thiourea, urea and dicyandiamide) displays irregular stacking of thick layers and massive particles [66–69]. This pristine g-C_3N_4 has small specific surface area and scanty pore structure. An effective strategy to obtain large specific surface area and pore volume is to add gas-producing compounds (such as water, ethanol, ammonium chloride and starch) during calcination [70–72]. By the orientation growth of melamine [73] or using oriented melem hydrate fibers as precursor [74], g-C_3N_4 with oriented structure was synthesized, and the unique oriented structure was beneficial for energy harvesting, conversion, and storage [75]. By using template and chemical/physical treatment of precursors or pristine g-C_3N_4, multifarious novel morphologies have been fabricated, including quantum dots [76–78], nanoribbon [79], nanofiber [80], nanotube [81], microsphere [82], nanosphere [83], microrod [84], nanorod [85,86] and micro string [87]. Unfortunately, although DFT calculation is good at modeling unit cell, it can hardly simulate various morphologies. On the one hand, same unit cell is shared by different morphologies. On the other hand, to construct a model resembling a specific morphology, the periodic boundary conditions are intractable, and amount of atoms in the constructed model will be too large to handle. Therefore, computational work dealing with novel morphology of g-C_3N_4 was only sporadically reported. For example, Zhai et al. constructed an equilateral triangle structure containing six heptazine units to simulate g-C_3N_4 quantum dot [88].

In 2009, Gracia et al. built C_3N_4 single-wall nanotube structures by curling up C_3N_4 single layers for the first time [89]. They inferred that the C_3N_4 nanotubes had a stable band gap of *ca.* 3.0 eV. Thereafter, other researchers further investigated the geometric structures and electronic properties of g-C_3N_4 nanotube from the perspective of novel photocatalyst [90–92]. In detail, two kinds of g-C_3N_4 nanotubes were constructed by rolling up g-C_3N_4 monolayer along the *x*-axis and *y*-axis, which were named as armchair and zigzag structures, and represented as (*n*, *n*) and (*m*, 0), respectively (Fig. 7a). Here, *m* and *n* were multiples of 3, and they represented the various diameters of g-C_3N_4 nanotubes. The band gap values of (*m*, 0) and (*n*, *n*) g-C_3N_4 nanotubes were smaller and larger than the experimental value (2.7 eV), respectively (Fig. 7b), and they got closer to 2.7 eV as *m* and *n* increased. The VBM of all g-C_3N_4 nanotubes were lower than that of g-C_3N_4 monolayer and the redox potential of O_2/H_2O (Fig. 7c). The CBM of all (*n*, *n*) and major (*m*, 0) g-C_3N_4 nanotubes were higher than the redox potentials of H^+/H_2 and CO_2/CH_4. In addition, the work functions of all g-C_3N_4 nanotubes were larger than that of g-C_3N_4 monolayer, and they decreased as *m* and *n* increased [91].

3.2. Non-metal doping

Non-metal doping is a widely employed approach to improve the photocatalytic activity of g-C_3N_4. So far, with the exception of As, Te

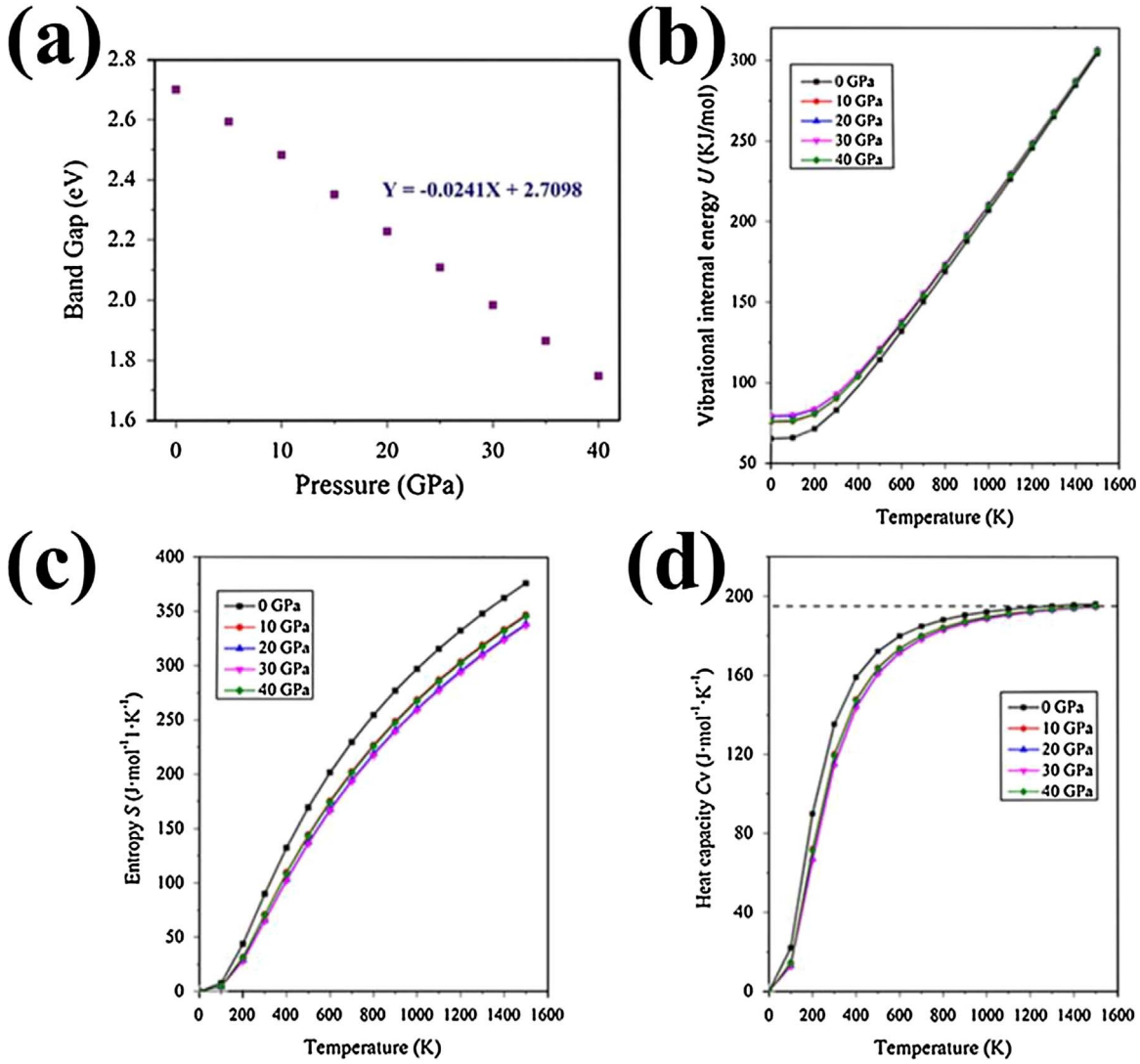

Fig. 6. (a) Variation of band gap of g-C_3N_4 *versus* pressure. (b) Vibrational internal energy, (c) entropy and (d) heat capacity of g-C_3N_4 at different temperatures and pressures. Reprinted with permission from Ref. [65]. Copyright 2014 Elsevier.

and At, all other non-metal elements in IIIA–VIIA groups have been experimentally introduced into g-C_3N_4 as doping elements. Overall, the introduction of these non-metal elements modifies the band gap, light absorption, specific surface area and separation efficiency of photo-generated electrons and holes, and therefore enhances the photocatalytic activity of g-C_3N_4 [93]. The changes in structural, electronic and optical properties are usually evidenced by experimental results, such as nitrogen adsorption–desorption isotherms, UV–vis diffuse reflection spectra and photoelectrochemical results [94]. However, the intrinsic reasons for these changes are difficult to examine by these methods. In this case, DFT calculation plays an irreplaceable role in investigating the properties of impurity-doped unit cell and understanding the photocatalytic activity enhancement mechanism at atomic and molecular levels.

To date, all non-metal elements in IA–VIIA groups (except At) doped g-C_3N_4 models have been investigated by DFT calculation. It should be noted that although As and Te doped g-C_3N_4 photocatalysts have not been synthesized yet, the computational research on As and Te doped g-C_3N_4 models has already been reported. This is because the construction of doping models is not restricted by experimental condition. The initial step in a computational research on doping system is devising doping models, which serves as the study object in the subsequent study. Dopant atoms can occupy substitutional or interstitial positions. As for tri-*s*-triazine-based g-C_3N_4, five substitutional sites and two interstitial sites are generally considered as doping sites (Fig. 8). The five substitutional sites are N1, N2, N3, C1 and C2 atoms. The two interstitial sites marked as I1 and I2 are a corner and the center of the sixfold cavity, respectively.

The actual doping site in a material can be deduced by experiments and calculations. The former is evaluating the chemical environment (valence and bonding state) of the impurity atom by experimental characterizations, such as Fourier transform infrared spectroscopy, X-ray photoelectron spectroscopy (XPS) and nuclear magnetic resonance. The latter is calculating and comparing the dopant formation energy (E_{form}) at different sites. In general, when E_{form} is more negative, the doping system is energetically more favorable. The former experimental method can exclude some doping sites and reduce calculation task. For example, the XPS spectrum of element X-doped g-C_3N_4 sample shows a peak attributed to X—C bond. Then the doping sites I1, I2, C1 and C2 can be excluded, and only the formation energy for the three N sites needs to be calculated. The formation energy of the doping system for the substitution and interstitial models is calculated using Eqs. (1) and (2), respectively.

$$E_{form} = E(\text{X-}C_3N_4) - E(C_3N_4) - \mu(X) + \mu(Y) \quad (1)$$

$$E_{form} = E(\text{X-}C_3N_4) - E(C_3N_4) - \mu(X) \quad (2)$$

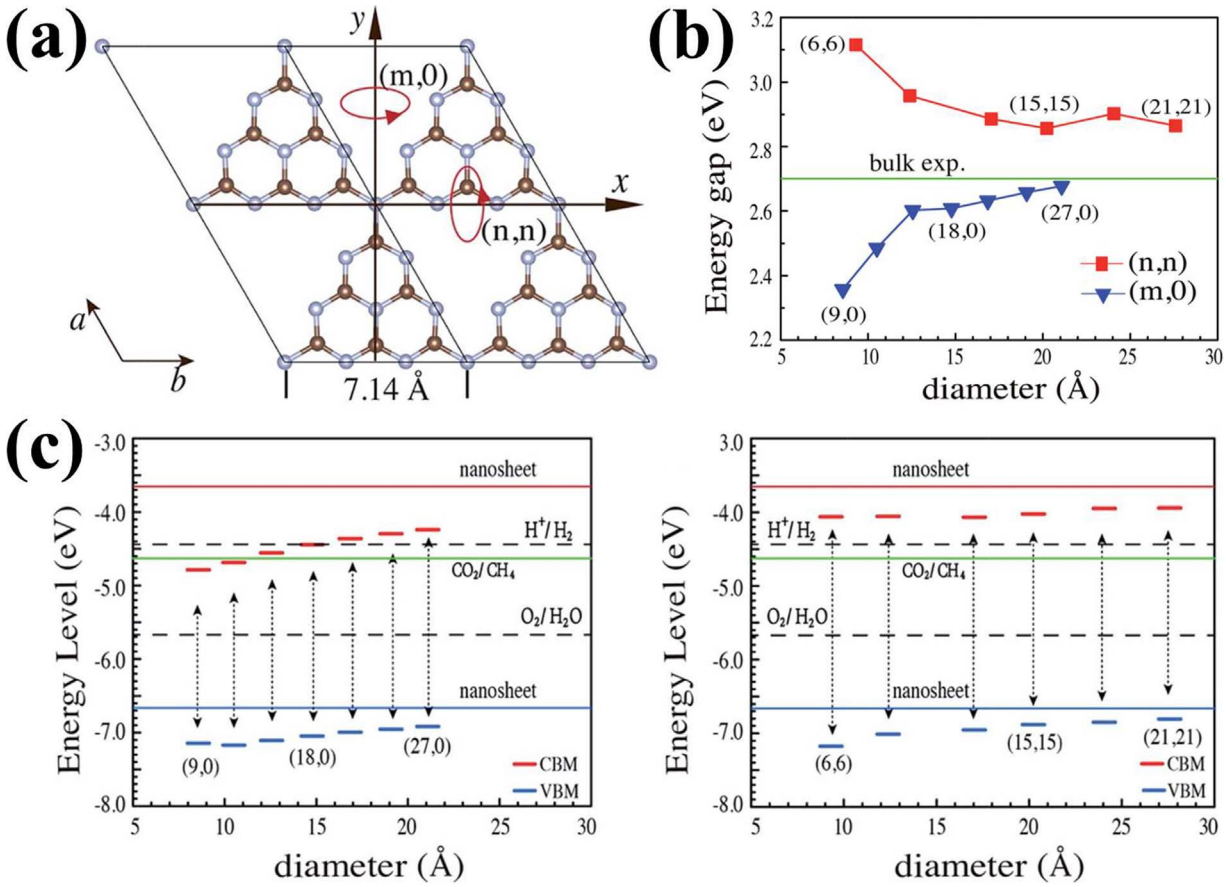

Fig. 7. (a) Schematic of curling up optimized g-C_3N_4 monolayer. (b) Energy gap and (c) band edge of (m, 0) and (*n*, *n*) g-C_3N_4 nanotubes. Reprinted with permission from Ref. [91]. Copyright 2017 Royal Society of Chemistry.

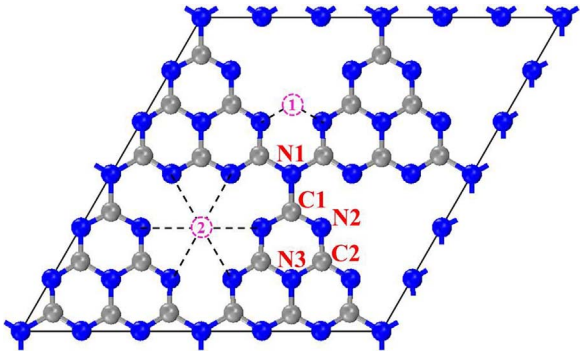

Fig. 8. Five substitutional sites and two interstitial sites in tri-*s*-triazine-based g-C_3N_4. The interstitial sites are marked by numbers 1 and 2 in purple circles. The dash lines are used to assist the presentation of sites 1 and 2 without physical meaning.

where E(X-C_3N_4) is the energy of element X-doped g-C_3N_4 system, E(C_3N_4) is the energy of pristine g-C_3N_4, μ(X) and μ(Y) are the chemical potentials of foreign atom X and substituted atom Y (Y = C, N), respectively.

In some computational reports on g-C_3N_4-based doping systems, the formation energy of the above doping sites was partially calculated and compared [42,95–98]. Table 1 compares typical formation energy for various doping systems. It is obvious that the formation energy at N2 site is more negative than that at other sites for O and S doped g-C_3N_4 systems. Analogously, for P doped g-C_3N_4 system, the formation energy at N2 site is also more negative than that at other N sites. In view of the above-mentioned observation, impurity atom in some reports was directly introduced into N2 site without comparing the formation energy at different doping sites [62,99–101]. Anyway, in all the computational

Table 1
Calculated formation energy (eV) of various non-metal elements doped g-C_3N_4 systems at different doping sites.

Impurity	N1	N2	N3	C1	C2	I1	Reference
O	0.51	−0.74	1.56	1.30	1.40		[95]
O	1.6	−0.9	0.7	5.3	4.8		[96]
P	1.93	1.33	3.55	0.73	1.52	0.78	[42]
S	4.00	1.76	6.43			2.12	[42]
S		3.41	7.26				[97]

reports on doping systems, the doping model was determined either by the formation energy or by the previous experience before investigating the properties.

The properties of doping systems examined in most literature include geometric structure, electronic and optical property. Ma et al. found that the introduction of S atom at N2 site and P atom at I1 site lowered the band gap of g-C_3N_4 from 2.70 eV to 2.10 eV and 2.01 eV, respectively (Fig. 9) [42]. Interestingly, DOS and molecular orbital analysis showed that the interstitial P atom offered a new channel (C—N—P—N—C) for the transfer of charge carriers between neighboring heptazine units. This result was also testified on P–Na co-doped g-C_3N_4 photocatalyst by Cao et al. [102]. Cui et al. concluded that O doping in g-C_3N_4 improved the visible light absorption and facilitated the delocalization of HOMO and LUMO [51]. Wang et al. discovered that the incorporation of F changed the HOMO and LUMO energy of g-C_3N_4 and thus modified the redox property [103]. Similar effect on orbital energy was also observed in the circumstance of P, B and S doped g-C_3N_4 systems [104–107]. Liu et al. analyzed the valence charge density in (100) and (101) planes of Cl-doped g-C_3N_4 system [108]. They declared that the intercalation of Cl atom strongly extended the localized 2D π-

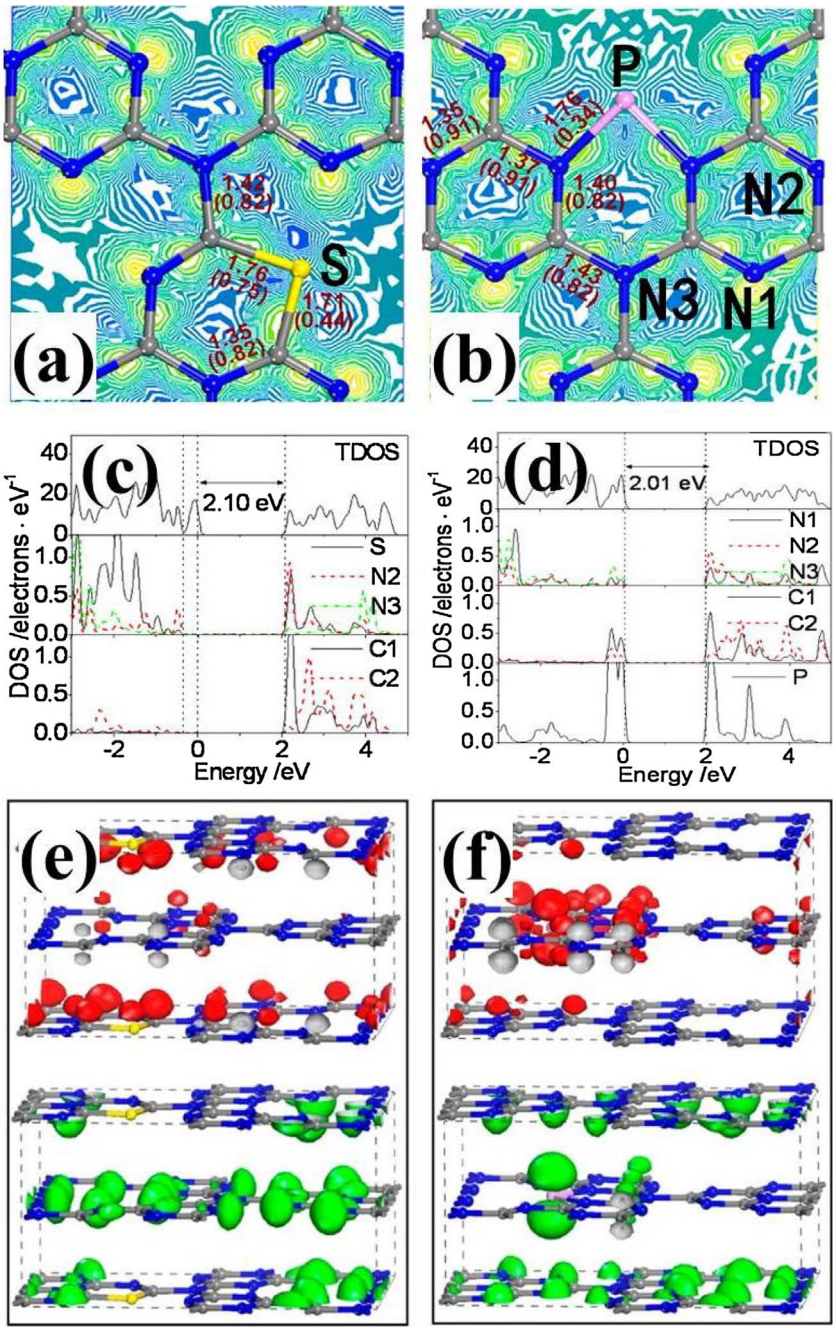

Fig. 9. Difference charge density contour maps (a, b), DOS (c, d), LUMO (red region) and HOMO (green region) (e, f) of S and P doped g-C_3N_4. The numbers with and without parenthesis in (a) and (b) are the bond overlap population and bond length (Å), respectively. The naming convention of nitrogen atoms in Ref. [42] is different with that in the present manuscript. The nitrogen atoms marked as N1, N2 and N3 in (b–d) are N2, N3 and N1 atoms in the present manuscript, respectively. Reprinted with permission from Ref. [42]. Copyright 2012 American Chemical Society. (For interpretation of the references to colour in this figure legend, the reader is referred to the web version of this article.)

conjugated system of g-C_3N_4 into 3D space. Ran et al. introduced P atom into g-C_3N_4 at C1 site [109]. DFT calculation results showed that the lattice distance (*a*) of g-C_3N_4 was enlarged after P incorporation, which agreed well with the X-ray diffraction result that the (100) peak moved to a smaller diffraction angle.

3.3. Metal doping

Metal doping is another effective approach employed in modifying the geometric and electronic structure of g-C_3N_4. As for the metal-doped g-C_3N_4 model, the substitution mode, namely replacing non-metal C and N atoms by metal atoms, is not taken into account because non-metal and metal are essentially different. Moreover, the I1 site is also unsuitable to embed metal atom since the space at I1 site is inadequate to accommodate metal atom with relatively larger radius. Gao et al. found that Pd and Pt atoms originally set at I1 site would spontaneously move to I2 site after geometry optimization [110]. Therefore, the metal atom was directly placed at I2 site in most literature on metal doped g-C_3N_4 system. Binding energy [111] and formation energy [55] are two different terms used to describe the energy change for the introduction of metal atoms into g-C_3N_4. But in both cases, the energy change is calculated using the same Eq. (2), and a more negative energy change indicates that the metal-doped g-C_3N_4 system is thermodynamically more stable. Table 2 summarizes the binding/formation energy of various metal-doped g-C_3N_4 systems at I2 site.

Ghosh et al. calculated the magnetic and optical property of 3d-transition metal (V, Cr, Mn, Fe, Co, Ni, Cu and Zn)-embedded g-C_3N_4 system [112]. The results showed that the introduction of these metal atoms not only induced a semiconductor to metal transition, but also facilitated light absorption. Hu et al. found that Fe^{3+} doping strongly enhanced the adsorption and activation of N_2 on g-C_3N_4 [115]. Xiong

Table 2
Binding/formation energy of various metal-doped g-C_3N_4 systems at I2 site.

Metal	Binding/formation energy (eV)	Reference	Metal	Binding/formation energy (eV)	Reference
V	−1.87	[112]	Cr	−3.65	[112]
Mn	−2.59, −4.48	[111,112]	Fe	−0.68	[112]
Co	1.4	[112]	Ni	1.97	[112]
Cu	2.1	[112]	Zn	1.4	[112]
Pd	−2.17	[110]	Pt	−2.95	[110]
Li	−4.477	[55]	Na	−4.144, −3.64	[55,113]
K	−3.603, −3.47	[55,113]	Pb	−3.56	[114]

et al. concluded that Na-doping favorably occurred on the I2 site at g-C_3N_4 in-plane, while K atom tended to intercalate into the g-C_3N_4 interlayer and bridge the adjacent layers (Fig. 10) [116]. Both Na and K doping narrowed the band gap of g-C_3N_4, but they exerted different influence on the electronic property of g-C_3N_4. Na doping increased the in-planar electron density and resulted in high recombination rate of charge carrier. K doping reduced the electronic localization and accelerated the charge carrier transfer between neighboring layers. The theoretical results convincingly elucidated the variation of photocatalytic activity by Na and K doping in their work. In another similar work, Zhu et al. discovered that the incorporation of alkali metal atoms (Li, Na and K) increased the work function of g-C_3N_4 from 4.42 eV to 5.94, 5.57 and 5.32 eV, respectively [55]. Li et al. replaced the terminal amino (−NH_2) in g-C_3N_4 by hydroxyl (−OH), and found that the incorporation of K in −OH replaced g-C_3N_4 was easier than that of Na [117].

3.4. g-C_3N_4–semiconductor

Numerous experiments indicated that a myriad of heterojunction photocatalysts composed of g-C_3N_4 and other semiconductors (sulfide, oxide, halide, tungstate, titanate, nitride, carbide, chromate, etc.) exhibited better photocatalytic activities than the unitary semiconductors because of the facilitated separation of photogenerated charge carriers [118–132]. Two common photocatalytic mechanisms, i.e. traditional type II heterojunction and direct Z-scheme, were usually employed to explicate the photogenerated charge carrier transfer process between different components in the composites [133–136].

The experimental method to distinguish these two mechanisms is firstly detecting the generation of hydroxyl radical (·OH) or superoxide radical ($\cdot O_2^-$) through electron spin resonance measurement [137] or through active species trapping experiment [138,139]. Followed by comparing the CB and VB potentials of each component with the standard redox potentials of $O_2/\cdot O_2^-$ and $\cdot OH/OH^-$, one can theoretically determine whether ·OH or $\cdot O_2^-$ can be generated in these two mechanisms, and thus negates one mechanism and confirms the other. Notably, this experimental method is not always practical for arbitrary composite photocatalysts. If the CB potentials of both components are simultaneously higher or lower than the redox potential of $O_2/\cdot O_2^-$, and the VB potentials of both components are simultaneously higher or lower than the redox potential of $\cdot OH/OH^-$, this experimental method becomes useless.

DFT investigation on composite photocatalysts mainly concentrates on the electronic property of the composite model. To date, the DFT investigation of g-C_3N_4-based composite photocatalyst is very limited, because it is difficult to construct an appropriate composite model for most composites. As for a composite of material A and material B, the success for constructing a composite model AB is dependent on how well their unit cells match. More specifically, the angles (α, *β*, and γ) of the unit cells of A and B must be equal, and the lattice constants in the *x*–*y* plane (*a* and *b*) of the unit cells of A and B must be similar. It is easy to equate the angles by selecting proper surface vectors when cleaving unit cell to build surface, while the match between lattice constants is sometimes difficult to realize. If the lattice constants of the unit cells of A and B differ dramatically, an effective solution is to build supercell by enlarging the pristine cell along *x* and *y* directions and then achieve the match between the lattice constants of the supercells. For example, the lattice constants of *s*-triazine-based g-C_3N_4 and MoS_2 are 4.79 and 3.19 Å, respectively. To build a g-C_3N_4/MoS_2 composite model, Wang et al. used a 2 × 2 supercell of *s*-triazine-based g-C_3N_4 and a 3 × 3 supercell of MoS_2 whose lattice constants were enlarged to 9.58 and 9.57 Å, respectively [140]. The mismatch of the enlarged lattice

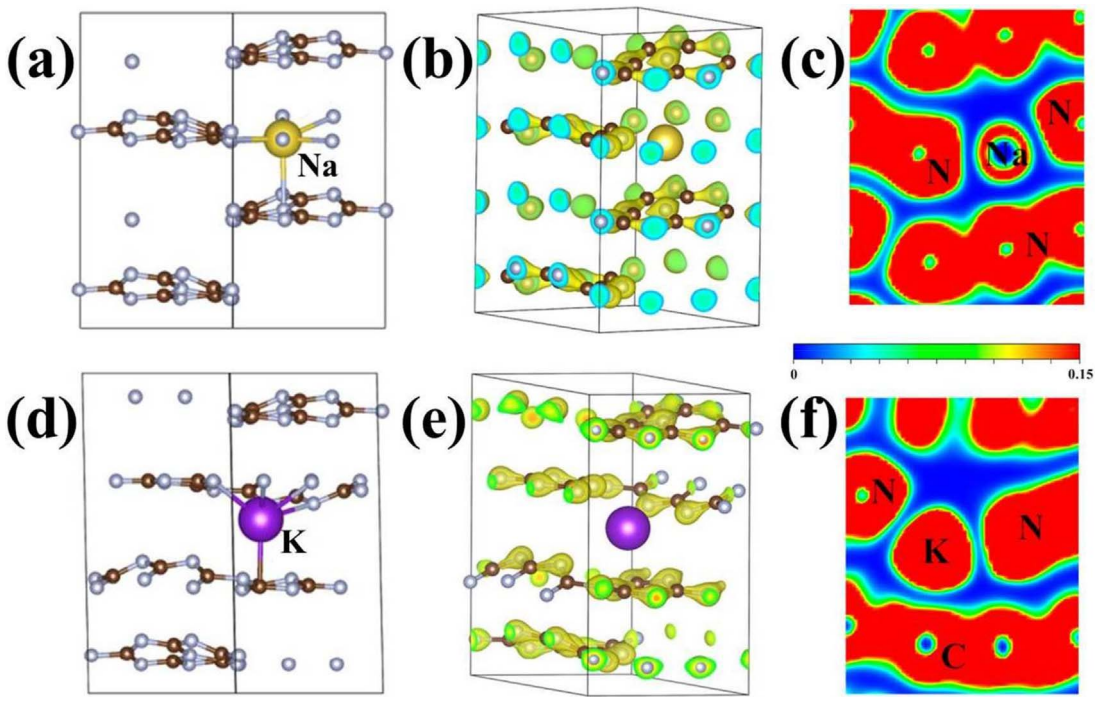

Fig. 10. Relaxed configurations (a, d), charge density (b, e) and electronic location function analysis (c, f) of Na and K doped g-C_3N_4. The isosurface in (b) and (e) is 2 e/Å^3. Reprinted with permission from Ref. [116]. Copyright 2016 American Chemical Society.

constants was only 1%. It seems that this method of creating supercell has comprehensive applicability as one can enlarge all the different lattice constants to the least common multiple and then the lattice constants of the supercells will be quite close, no matter how much disparity exists in the pristine lattice constants. However, practical consideration is that a highly enlarged supercell will certainly contain plenty of atoms, and the resultant composite model is beyond simulation due to the numerical cost.

Back to the classification of traditional type II heterojunction and direct Z-scheme photocatalytic mechanisms, a mature method based on DFT calculation has been developed to identify them in various composites. This method is closely related to the work function, Fermi energy, together with CB and VB potentials of each component. To quickly apprehend this method, the DFT investigation of g-C_3N_4/CdS composite performed by Liu can be taken as a typical example [141]. At first, the work functions of g-C_3N_4, CdS and g-C_3N_4/CdS were calculated to be 4.34, 5.04 and 4.51 eV, respectively (Fig. 11a). The work function of g-C_3N_4 was smaller than that of CdS, indicating that the Fermi energy of g-C_3N_4 (−4.34 eV *vs.* AVS) was higher than that of CdS (−5.04 eV *vs.* AVS). When g-C_3N_4 came into contact with CdS, the electrons in g-C_3N_4 would transfer to CdS, thus forming an electric field between g-C_3N_4 and CdS. The direction of this electric field was from g-C_3N_4 to CdS. As a result, the Fermi energy of CdS and g-C_3N_4 shifted to the same value (−4.51 eV *vs.* AVS). This led to an upward and downward shift of 0.53 eV and 0.17 eV in the Fermi energy of CdS and g-C_3N_4, respectively. In this process, the band edge potentials of CdS and g-C_3N_4 also underwent the same shifting behavior as the Fermi energy. The resultant CB and VB potentials of CdS were −1.03 and 1.33 eV *vs.* NHE, and the corresponding CB and VB potentials of g-C_3N_4 were situated at −0.98 and 1.78 eV *vs.* NHE, respectively. Upon irradiation, since the direction of the electric field was from g-C_3N_4 to CdS, the transfer mode of charge carriers should be the transfer of photogenerated electrons from the CB of CdS to g-C_3N_4. Given that the resultant CB of CdS was higher than that of g-C_3N_4, it can be further inferred that the photogenerated electrons in the CB of CdS would transfer to the CB of g-C_3N_4. Therefore, a photocatalytic mechanism of traditional type II heterojunction was adjudged for the g-C_3N_4/CdS composite. It was noted that the abovementioned electron transfer before light irradiation was inferred by the comparison of work function and Fermi energy. In fact, it can also be illustrated intuitively by charge density difference (Fig. 11b and c).

To summarize, the above method is universal and can be extended to other binary composites composed of semiconductor A and semiconductor B. Initially, the work functions of model A, model B and

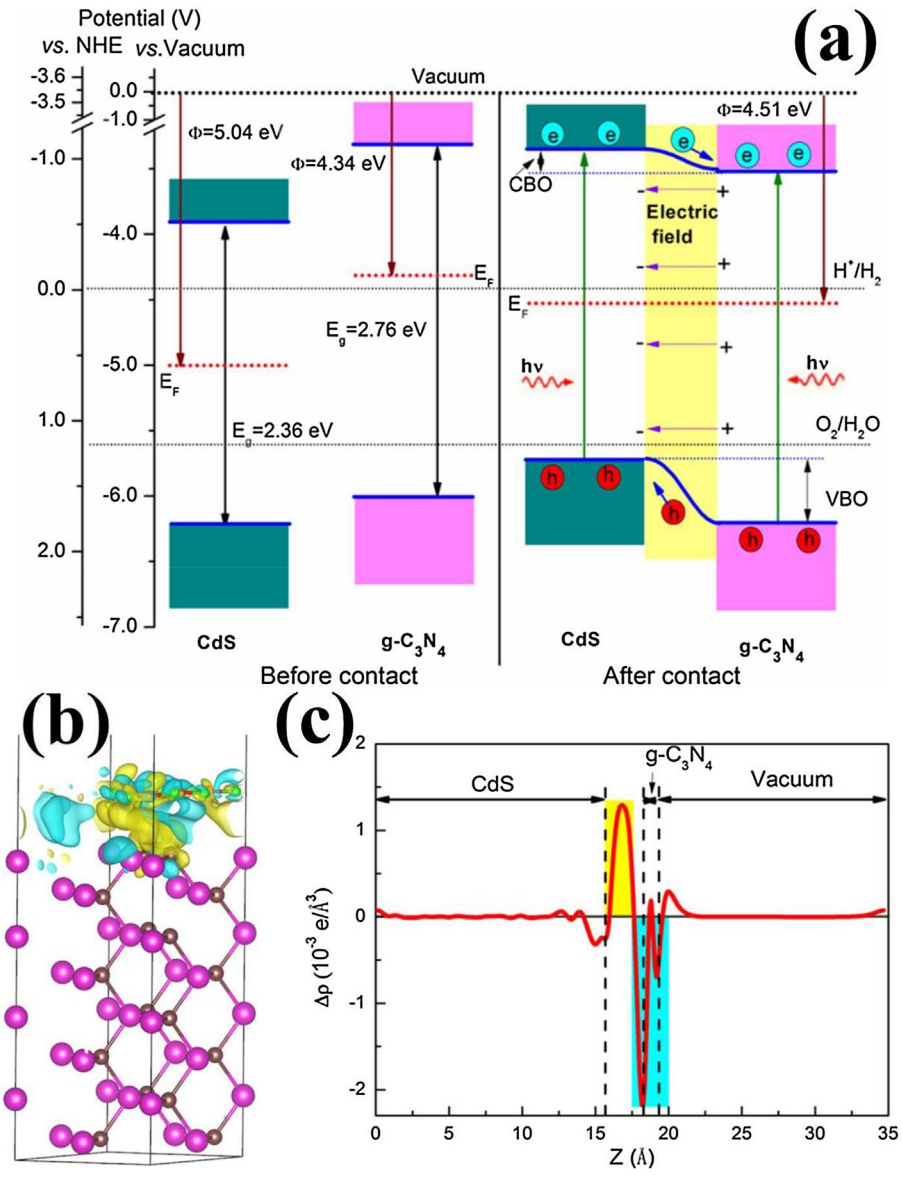

Fig. 11. (a) Diagram of the band edge positions before and after contact of g-C_3N_4 and CdS. (b) Charge density difference (0.0004 e/Å^3) and (c) planar-averaged electron density difference of g-C_3N_4/CdS composite model. The yellow and cyan regions represent electron accumulation and depletion, respectively. Reprinted with permission from Ref. [141]. Copyright 2015 American Chemical Society. (For interpretation of the references to colour in this figure legend, the reader is referred to the web version of this article.)

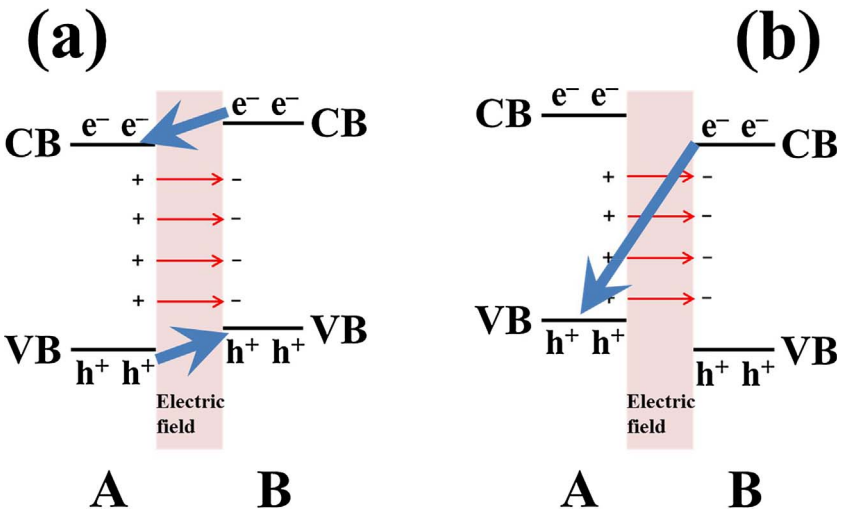

Fig. 12. Diagram of photogenerated charge carriers transfer mode in traditional type II heterojunction (a) and direct Z-scheme (b) photocatalytic mechanisms. The blue arrows indicate the transfer routes of photogenerated charge carriers. (For interpretation of the references to colour in this figure legend, the reader is referred to the web version of this article.)

composite model AB are compared. If the work function of A is smaller than that of B, the electrons in A will transfer to B. As a result, an electric field pointing from A to B is formed and the Fermi energies of A and B will shift to the same value (the Fermi energy of AB). The second step is judging the shift direction and scale of the Fermi energies and band edge potentials of A and B. The last step is calculating and comparing the resultant band edge potentials of A and B. Under light irradiation, since the electric field is from A to B, the transfer mode of charge carriers should be the transfer of photogenerated electrons from the CB of B to A. If the resultant CB of B is higher than that of A, it can be further inferred that the photogenerated electrons in the CB of B will transfer to the CB of A, and the photocatalytic mechanism can be ascertained to be traditional type II heterojunction (Fig. 12a). Contrarily, if the resultant CB of B is lower than that of A, it can be further inferred that the photogenerated electrons in the CB of B will transfer to the VB of A, and the photocatalytic mechanism becomes direct Z-scheme instead (Fig. 12b).

The above "work function-band edge" method has also been successfully adopted in investigating the photocatalytic mechanism for other composites such as g-C_3N_4/$BiVO_4$ [58] and g-C_3N_4/Zn_2GeO_4 [59]. Some key points can be summarized as follows. (1) The decisive factors for the photocatalytic mechanism are work function and the relative location of the shifted band edge potential, which determine how and where the transfer and accumulation of the photogenerated electrons occur, respectively. (2) Two kinds of electron transfer will take place before and under light irradiation. The directions of these two transfer processes are opposite. The one before light irradiation can be evidenced by experimental characterization XPS [142–144]; while the one under light irradiation is the transfer of photogenerated electrons. (3) Whether the semiconductors in the composite are p-type or n-type is not addressed in this method.

3.5. g-C_3N_4–carbon-based materials

Carbon-based materials serve as excellent skeletons, co-catalysts, electron acceptors and photo-sensitizers in photocatalysis systems [145–148]. The common carbon-based materials employed to enhance the photocatalytic activity of g-C_3N_4 include amorphous carbon [149], graphene [150], graphene oxide [151], carbon black [152], fullerene (C_{60}) [153], carbon quantum dot [154] and carbon nanodot [155]. DFT investigation on g-C_3N_4-carbon-based materials composites aims to reveal the underlying activity enhancement mechanism. Du et al. disclosed a strong electronic coupling at graphene/g-C_3N_4 interface [156]. The charge transferred from graphene to g-C_3N_4, thus increasing the electron conductivity of g-C_3N_4 and promoting the oxygen reduction reaction. Meanwhile, the graphene/g-C_3N_4 composite exhibited stronger visible light absorption compared to prinstine g-C_3N_4. Gao et al. discovered that the decoration of carbon nanodots on g-C_3N_4 reduced the band gap, facilitated the separation of photogenerated charge carriers and red-shifted the optical absorption spectrum [157]. Furthermore, the carbon nanodots also acted as spectral sensitizer in the composite for water splitting. Li et al. constructed C_{60}/g-C_3N_4 hybrid models by placing a single C_{60} molecule above g-C_3N_4 monolayer at N1, N3 and I2 sites [158]. The adhesive energies for these models indicated that the most favorable adhesion site was I2 (Fig. 13a and b). The adhesion of C_{60} molecule at I2 site enhanced the optical absorption (Fig. 13c) and assisted effective charge separation. The traditional type II heterojunction mechanism was proposed to interpret the charge transfer route (Fig. 13d).

3.6. g-C_3N_4–organic molecule

Organic molecules were also introduced into g-C_3N_4 to modify the distribution of molecular orbital and orbital energy. Gong et al. grafted pyromellitic dianhydride (PMDA) into g-C_3N_4 to construct polyimide (PI), which changed the location of LUMO from heptazine to the PMDA moiety (Fig. 14) [159]. The resultant different location of LUMO and HOMO was beneficial for the spatial charge separation. Moreover, the CB and VB of PI were lower than those of g-C_3N_4, which created prerequisites for the formation of traditional type II heterojunction between g-C_3N_4 and PI. In addition, the energies of LUMO and HOMO of PI were also demonstrated to be lower than those of g-C_3N_4 by Chu et al. [160]. Similarly, Chen et al. reported the locational change of HOMO and orbital energy variation in 2,6-diaminopyridine-doped g-C_3N_4 system [161].

4. Photocatalytic reaction on tri-*s*-triazine-based g-C_3N_4

4.1. Adsorption of small molecule

The photocatalytic reactions performed by g-C_3N_4 photocatalyst include NO removal [162,163], water splitting [164,165], CO_2 reduction [166,167] and organic pollutant degradation [168–170]. The reactants in these reactions are NO, O_2, H_2O, CO_2 and organic dyes. As the first step in photocatalytic reactions, the adsorption of reactants on the surface of photocatalysts is extremely vital since it is closely associated with the subsequent reactions. Despite that experimental method is adept at measuring the adsorption amount of gas molecules and organic dyes, the concrete adsorption details (adsorption site, separation distance and adsorption intensity) are more suitable to be examined by DFT calculation. Analogous to the approach of element doping, various adsorption models need to be designed first, and then the adsorption

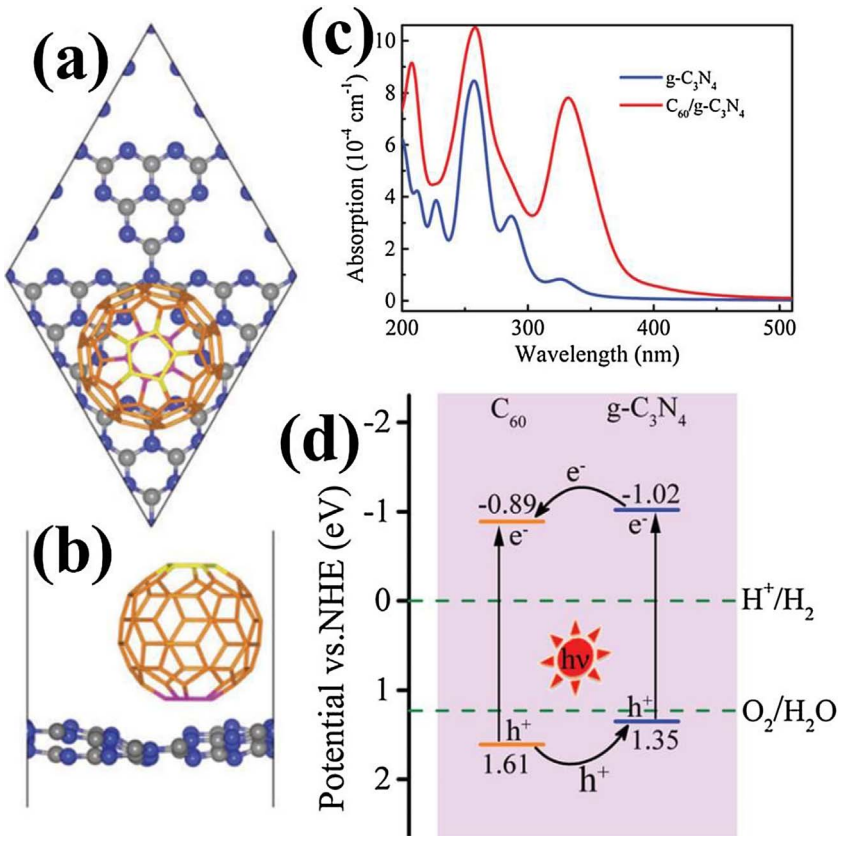

Fig. 13. (a) Top view and (b) side view of optimized C_{60}/g-C_3N_4 model. (c) Optical absorption spectra of g-C_3N_4 and C_{60}/g-C_3N_4. (d) Proposed charge transfer route between C_{60} and g-C_3N_4. Reprinted with permission from Ref. [158]. Copyright 2016 Royal Society of Chemistry.

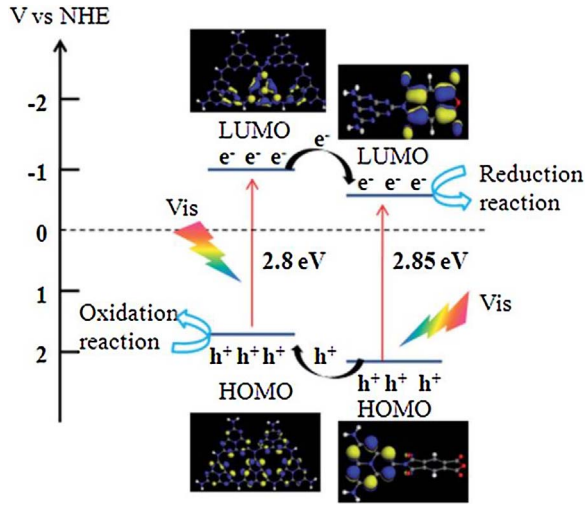

Fig. 14. Diagram of charge separation between g-C_3N_4 and PI. The red and white spheres are O and H atoms, respectively. Reprinted with permission from Ref. [159]. Copyright 2015 Royal Society of Chemistry. (For interpretation of the references to colour in this figure legend, the reader is referred to the web version of this article.)

energy (E_{ads}) is calculated and compared to determine the most stable adsorption system.

There are eleven adsorption sites in the g-C_3N_4 tri-*s*-triazine-based structure, including five atom sites, two interstitial sites and four bond sites (Fig. 15). The five atom sites are N1, N2, N3, C1 and C2 atoms. The two interstitial sites marked as I2 and I3 are the centers of the sixfold cavity and the *s*-triazine unit, respectively. The four bond sites marked as B1, B2, B3 and B4 are the midpoints of N1–C1, C1–N2, N2–C2 and C2–N3 bonds, respectively. The adsorption models are built by placing single small molecules above the g-C_3N_4 surface at these sites. The adsorbed small molecules can be parallel or vertical to the g-C_3N_4 plane, and the separation distance between the adsorbate and the g-C_3N_4 plane is variable. The adsorption energy of the adsorption system is calculated using $E_{ads} = E(M–C_3N_4) - E(C_3N_4) - E(M)$, where M is the adsorbate, $E(M)$ and $E(M–C_3N_4)$ are the energies of the adsorbate and whole adsorption system, respectively. A negative E_{ads} indicates that the adsorption process is exothermic and the adsorption system is stable. The common unit of E_{ads} is eV, though kJ mol^{-1} is also rarely used [171,172].

Aspera et al. calculated the adsorption energies of H_2O and O_2 on g-C_3N_4 at these sites [173,174]. It turned out that the most stable adsorption sites for H_2O and O_2 were N2 and B4 sites, respectively. The corresponding adsorption energies were −0.716 and −0.5825 eV, respectively. The adsorption of H_2O and O_2 made the pristine planar structure of g-C_3N_4 corrugated. Meanwhile, DOS analysis showed that H_2O adsorbed g-C_3N_4 system had a larger band gap than pristine g-C_3N_4. Wu et al. also observed an increase in band gap resulted by the adsorption of H_2O on g-C_3N_4 (Fig. 16a) [175]. This increase was accompanied with the down-shifted CB and VB edges; while the photocatalytic ability of H_2 production remained. The adsorption energy of the H_2O adsorbed g-C_3N_4 system in their work was −0.52 eV. Moreover, it was found that the average adsorption energy increased with the numbers of adsorbed H_2O molecules (Fig. 16b), which was due to the formation of hydrogen bonds between adjacent H_2O molecules (Fig. 16c). Interestingly, the adsorption energy of H_2O adsorbed graphene/g-C_3N_4 system was calculated to be −0.58 eV in another work of Wu [176], which was more negative than that of H_2O adsorbed g-C_3N_4 system. This result provided a support for the better photocatalytic H_2 production activity of graphene/g-C_3N_4 composite than that of pristine g-C_3N_4 in terms of the adsorption of reactant. Besides, Wu et al. further investigated the influence of defect on the adsorption of water on g-C_3N_4 [177]. The defect was created by purposely removing a heptazine unit in a 2 × 2 g-C_3N_4 supercell. And it suggested that, after adsorption on defect-containing g-C_3N_4, water trimer was easier to be stabilized than single water molecule, water dimer and tetramer.

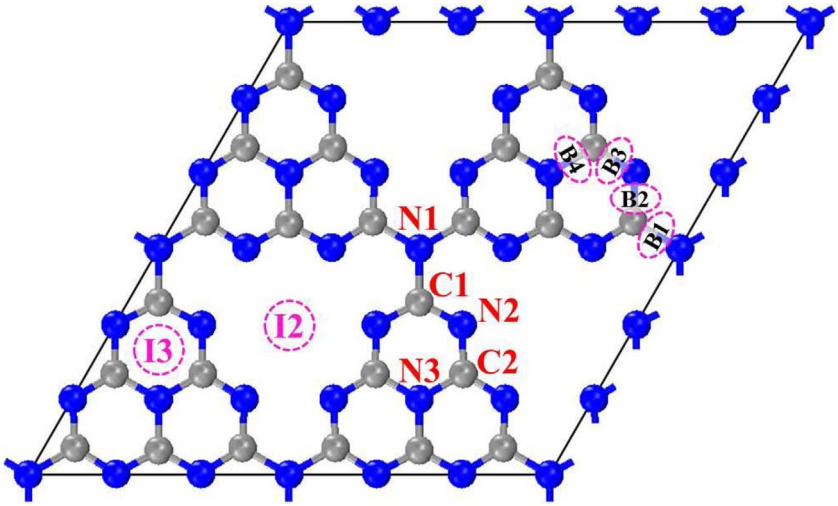

Fig. 15. Eleven adsorption sites in tri-*s*-triazine-based g-C_3N_4.

Our previous work investigated the adsorption energy of CO_2 on g-C_3N_4 at the aforementioned eleven adsorption sites and it was identified that the most stable site for CO_2 was N2 [178]. Similarly, the adsorption of CO_2 also engendered a corrugated g-C_3N_4 structure and an increased band gap. Stable adsorption configurations can be achieved with an initial separation distance of 1–4 Å. Ji et al. reported that the adsorption energies of H_2O, CO_2, H_2, N_2, CO, and CH_4 on g-C_3N_4 were −0.513, −0.226, −0.078, −0.117, −0.155 and −0.163 eV, respectively [179]. Among them, only CH_4 tended to adsorb at I3 site, while the other five molecules preferred to adsorb at the sixfold cavity (Fig. 17). Intriguingly, the adsorption energies of the reactants (H_2O and CO_2) in photocatalytic reactions were more negative than those of the products (H_2, CO, and CH_4), indicating the strong adsorption of reactants onto g-C_3N_4 and easy desorption of products from g-C_3N_4, which were strikingly advantageous to initiate the reaction and re-expose adsorption sites, respectively. Xia et al. corroborated that monolayer g-C_3N_4 had better CO_2 adsorption ability than multilayer g-C_3N_4 [180]. Sun et al. obtained adsorption energy of −0.76 eV for the adsorption of H_2CO_3 on g-C_3N_4 [113].

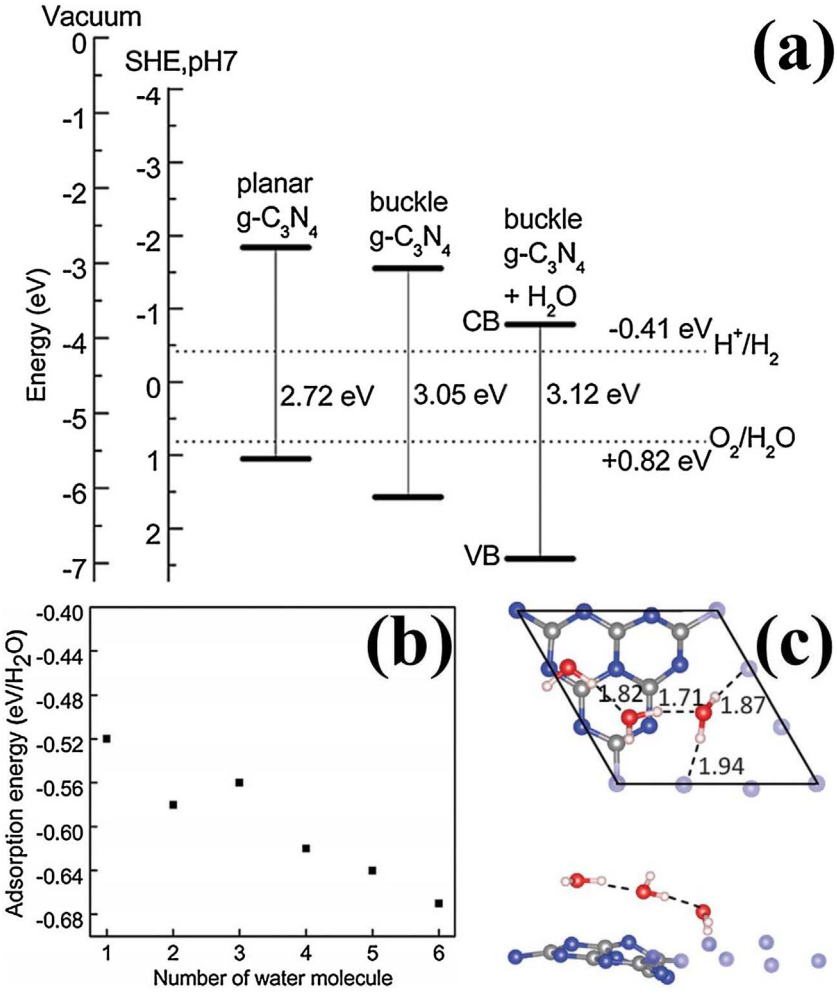

Fig. 16. (a) Band edge potentials of pristine and H_2O-adsorbed g-C_3N_4. (b) Adsorption energy of various numbers of H_2O-adsorbed g-C_3N_4. (c) Top view (upper) and side view (lower) of trimer water-adsorbed g-C_3N_4. The dashed lines represent hydrogen bonds and the numbers are the lengths of the hydrogen bonds. Reprinted with permission from Ref. [175]. Copyright 2014 Royal Society of Chemistry.

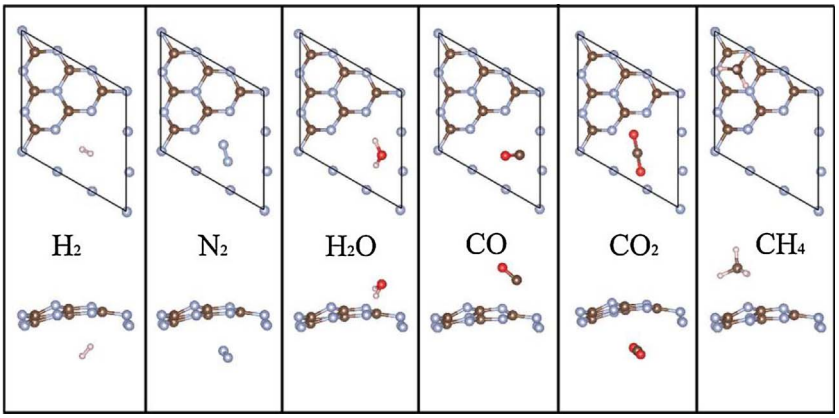

Fig. 17. Optimized adsorption configurations of H_2, N_2, H_2O, CO, CO_2 and CH_4 on g-C_3N_4. Reprinted with permission from Ref. [179]. Copyright 2016 Royal Society of Chemistry.

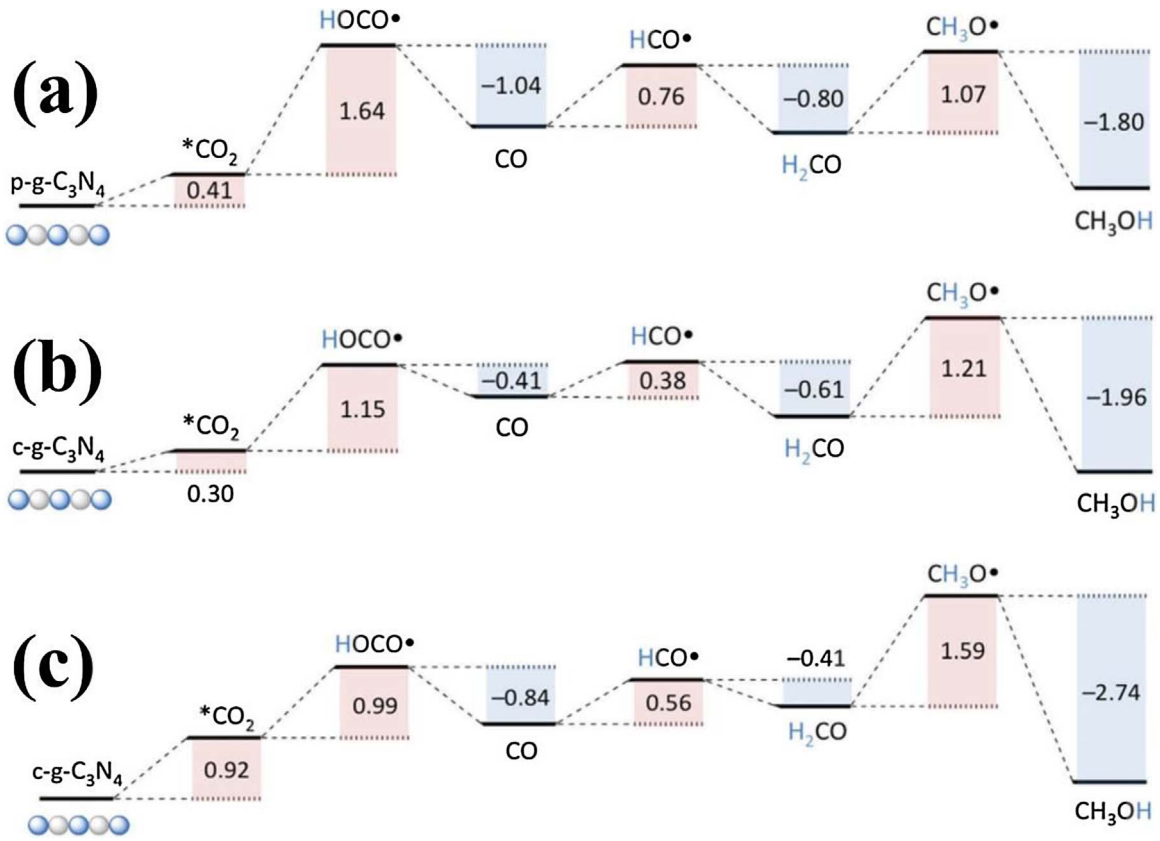

Fig. 18. Gibbs free energy diagram of the CO_2 conversion processes on (a) planar and (b) corrugated g-C_3N_4. (c) Gibbs free energy diagram of the CO_2 conversion process on corrugated g-C_3N_4 in the presence of 13 H_2O molecules. Reprinted with permission from Ref. [183]. Copyright 2016 Royal Society of Chemistry.

4.2. Photocatalytic water splitting on g-C_3N_4

Photocatalytic water splitting contains two half reactions, O_2 generation via H_2O oxidation and H_2 generation via H^+ reduction. The standard redox potentials of O_2/H_2O and H^+/H_2 are 1.23 and 0 eV *vs.* NHE, respectively. And both of the redox potentials perfectly lie within the VB and CB potentials of g-C_3N_4, creating a straddling band edge position, which theoretically enables g-C_3N_4 to catalyze the overall water splitting. However, experimental results manifested that cocatalyst and sacrificial agent were still indispensable to trigger the photocatalytic reactions, which was due to the intrinsic overpotential and rapid combination of photogenerated charge carriers. Wirth et al. investigated the two half reactions in water splitting on g-C_3N_4 by DFT calculation [181]. They found that the rate-limiting step in the H_2O oxidation process was the dissociation of H_2O from g-C_3N_4, and the overpotential was as high as 1.56 eV. As for the H_2 generation process, the overpotential was so small that it could be readily provided by photogenerated electrons. To conclude, O_2 generation process demands oxidation cocatalyst, while H_2 production can be simply attained without the aid of cocatalyst. Fu et al. examined the hydrogen evolution reaction (HER) on MoS_2/g-C_3N_4 composite [182]. The calculated free energy of hydrogen atom adsorption on MoS_2/g-C_3N_4 (−0.17 eV) was closer to 0 than that on pristine g-C_3N_4 (−0.52 eV), which well explained the excellent HER activity of MoS_2/g-C_3N_4 composite.

4.3. Photocatalytic CO_2 reduction on g-C_3N_4

Photocatalytic CO_2 reduction is a complicated reaction which involves several intermediate steps and generates various products such as CO, CH_4, CH_3OH, HCHO and HCOOH. The reaction pathway and primary products are determined through scrutinizing the variation of free energy in the assumed reaction process by DFT method. Azofra

et al. compared the CO_2 conversion processes on planar g-C_3N_4 (p-g-C_3N_4) and corrugated g-C_3N_4 (c-g-C_3N_4) [183]. The rate-limiting steps for p-g-C_3N_4 and c-g-C_3N_4 were the hydrogenations of adsorbed CO_2 and generated H_2CO, corresponding to energy inputs of 1.64 and 1.21 eV, respectively (Fig. 18a and b). As a result, the main products of the CO_2 reduction reaction on p-g-C_3N_4 and c-g-C_3N_4 were CH_3OH and CO, respectively. When 13 H_2O molecules were introduced, the energy input for the hydrogenation of H_2CO on c-g-C_3N_4 increased to 1.59 eV, and more energy (0.84 eV) was released in the formation process of CO (Fig. 18c), thus augmenting the potential for generating CO as a product on c-g-C_3N_4. Gao et al. investigated the reaction pathways for CO_2 reduction on Pt and Pd co-catalyzed g-C_3N_4 [110]. The rate-limiting steps for Pd/g-C_3N_4 and Pt/g-C_3N_4 were the hydrogenation of adsorbed CH_2OH and HCOOH, corresponding to energy barriers of 1.46 and 1.16 eV, respectively. Consequently, the favored products of the CO_2 reduction reaction on Pt/g-C_3N_4 and Pd/g-C_3N_4 were CH_4 and HCOOH, respectively.

5. Summary and outlook

The structural, electronic and optical properties of tri-*s*-triazine-based g-C_3N_4 have been sufficiently disclosed by DFT calculations. The effect of morphology, elemental doping, carbon incorporation and hybridization with other semiconductors on the properties and photocatalytic activities of tri-*s*-triazine-based g-C_3N_4 were also thoroughly investigated.

However, detailed theoretical calculations on tri-*s*-triazine-based g-C_3N_4 on the following aspects are still underway and desired to be accomplished. (1) Additional composites models should be constructed by tactfully selecting suitable lattice plane and surface vector, thus providing theoretical support for other g-C_3N_4-based composites. (2) The adsorption of other small molecules and ions on tri-*s*-triazine-based g-C_3N_4 needs to be examined. (3) At present, the contribution of DFT calculation to the explanation of enhanced photocatalytic activity of modified g-C_3N_4 mainly focuses on the electronic properties. Meanwhile, reaction thermodynamics and pathways revealed by DFT calculation are other directions for the interpretation of the photocatalytic activity enhancement.

Acknowledgments

This work was supported by NSFC (51320105001, 51372190, 21573170 and 21433007), 973 program (2013CB632402), NSFHP (2015CFA001), Innovative Research Funds of SKLWUT (2017-ZD-4) and the Fundamental Research Funds for the Central Universities (WUT: 2017-YB-002 and 2015-III-034).

References

[1] A.Y. Liu, M.L. Cohen, Prediction of new low compressibility solids, Science 245 (1989) 841–842.
[2] J.L. Corkill, M.L. Cohen, Calculated quasiparticle band gap of β-C_3N_4, Phys. Rev. B 48 (1993) 17622–17624.
[3] A.Y. Liu, R.M. Wentzcovitch, Stability of carbon nitride solids, Phys. Rev. B 50 (1994) 10362–10365.
[4] D.M. Teter, R.J. Hemley, Low-compressibility carbon nitrides, Science 271 (1996) 53–55.
[5] I. Alves, G. Demazeau, B. Tanguy, F. Weill, On a new model of the graphitic form of C_3N_4, Solid State Commun. 109 (1999) 697–701.
[6] S.F. Matar, M. Mattesini, *Ab initio* search of carbon nitrides isoelectronic with diamond, likely to lead to new ultra hard materials, Comptes Rendus de l'Académie des Sci.—Ser. IIC—Chem. 4 (2001) 255–272.
[7] T. Komatsu, Prototype carbon nitrides similar to the symmetric triangular form of melon, J. Mater. Chem. 11 (2001) 802–805.
[8] Y. Xu, S. Gao, Band gap of C_3N_4 in the GW approximation, Int. J. Hydrogen Energy 37 (2012) 11072–11080.
[9] E. Kroke, M. Schwarz, E. Horath-Bordon, P. Kroll, B. Noll, A.D. Norman, Tri-s-triazine derivatives. Part I. From trichloro-tri-s-triazine to graphitic C_3N_4 structures, New J. Chem. 26 (2002) 508–512.
[10] X. Wang, K. Maeda, A. Thomas, K. Takanabe, G. Xin, J.M. Carlsson, K. Domen, M. Antonietti, A metal-free polymeric photocatalyst for hydrogen production from water under visible light, Nat. Mater. 8 (2009) 76–80.
[11] Y. Li, L. Yang, G. Dong, W. Ho, Mechanism of NO photocatalytic oxidation on g-C_3N_4 was changed by Pd-QDs modification, Molecules 21 (2015) 36.
[12] H. Li, X. Wu, S. Yin, K. Katsumata, Y. Wang, Effect of rutile TiO_2 on the photocatalytic performance of g-C_3N_4/brookite-$TiO_{2-x}N_y$ photocatalyst for NO decomposition, Appl. Surf. Sci. 392 (2017) 531–539.
[13] J.A. Singh, S.H. Overbury, N.J. Dudney, M. Li, G.M. Veith, Gold nanoparticles supported on carbon nitride: influence of surface hydroxyls on low temperature carbon monoxide oxidation, ACS Catal. 2 (2012) 1138–1146.
[14] C. Lu, R. Chen, X. Wu, M. Fan, Y. Liu, Z. Le, S. Jiang, S. Song, Boron doped g-C_3N_4 with enhanced photocatalytic UO_2^{2+} reduction performance, Appl. Surf. Sci. 360 (2016) 1016–1022.
[15] L. Zhou, L. Wang, J. Lei, Y. Liu, J. Zhang, Fabrication of TiO2/Co-g-C3N4 heterojunction catalyst and its photocatalytic performance, Catal. Commun. 89 (2017) 125–128.
[16] M. Aleksandrzak, W. Kukulka, E. Mijowska, Graphitic carbon nitride/graphene oxide/reduced graphene oxide nanocomposites for photoluminescence and photocatalysis, Appl. Surf. Sci. 398 (2017) 56–62.
[17] S. Lam, J. Sin, A.R. Mohamed, A review on photocatalytic application of g-C_3N_4/semiconductor (CNS) nanocomposites towards the erasure of dyeing wastewater, Mater. Sci. Semicond. Process. 47 (2016) 62–84.
[18] T. Yu, L. Liu, F. Yang, Heterojunction between anodic TiO_2/g-C_3N_4 and cathodic WO_3/W nano-catalysts for coupled pollutant removal in a self-biased system, Chin. J. Catal. 38 (2017) 270–277.
[19] Q. Xu, C. Jiang, B. Cheng, J. Yu, Enhanced visible-light photocatalytic H_2-generation activity of carbon/g-C_3N_4 nanocomposites prepared by two-step thermal treatment, Dalton Trans. 46 (2017) 10611–10619.
[20] W. Iqbal, B. Qiu, J. Lei, L. Wang, J. Zhang, M. Anpo, One-step large-scale highly active g-C_3N_4 nanosheets for efficient sunlight-driven photocatalytic hydrogen production, Dalton Trans. 46 (2017) 10678–10684.
[21] K. Li, F. Su, W. Zhang, Modification of g-C_3N_4 nanosheets by carbon quantum dots for highly efficient photocatalytic generation of hydrogen, Appl. Surf. Sci. 375 (2016) 110–117.
[22] S. Ye, R. Wang, M. Wu, Y. Yuan, A review on g-C_3N_4 for photocatalytic water splitting and CO_2 reduction, Appl. Surf. Sci. 358 (2015) 15–27.
[23] S. Liu, F. Chen, S. Li, X. Peng, Y. Xiong, Enhanced photocatalytic conversion of greenhouse gas CO_2 into solar fuels over g-C_3N_4 nanotubes with decorated transparent ZIF-8 nanoclusters, Appl. Catal. B: Environ. 211 (2017) 1–10.
[24] H. Li, Y. Gao, X. Wu, P. Lee, K. Shih, Fabrication of heterostructured g-C_3N_4/Ag-TiO_2 hybrid photocatalyst with enhanced performance in photocatalytic conversion of CO_2 under simulated sunlight irradiation, Appl. Surf. Sci. 402 (2017) 198–207.
[25] S. Cao, J. Yu, g-C_3N_4-based photocatalysts for hydrogen generation, J. Phys. Chem. Lett. 5 (2014) 2101–2107.
[26] H. Li, L. Wang, Y. Liu, J. Lei, J. Zhang, Mesoporous graphitic carbon nitride materials: synthesis and modifications, Res. Chem. Intermed. 42 (2015) 3979–3998.
[27] Q. Fan, J. Liu, Y. Yu, S. Zuo, B. Li, A simple fabrication for sulfur doped graphitic carbon nitride porous rods with excellent photocatalytic activity degrading RhB dye, Appl. Surf. Sci. 391 (2017) 360–368.
[28] N. Sagara, S. Kamimura, T. Tsubota, T. Ohno, Photoelectrochemical CO_2 reduction by a p-type boron-doped g-C_3N_4 electrode under visible light, Appl. Catal. B: Environ. 192 (2016) 193–198.
[29] P. Chen, K. Li, Y. Yu, W. Zhang, Cobalt-doped graphitic carbon nitride photocatalysts with high activity for hydrogen evolution, Appl. Surf. Sci. 392 (2017) 608–615.
[30] Q. Xiang, J. Yu, M. Jaroniec, Preparation and enhanced visible-light photocatalytic H_2-production activity of graphene/C_3N_4 composites, J. Phys. Chem. C 115 (2011) 7355–7363.
[31] F. Cheng, H. Yin, Q. Xiang, Low-temperature solid-state preparation of ternary CdS/g-C_3N_4/CuS nanocomposites for enhanced visible-light photocatalytic H_2-production activity, Appl. Surf. Sci. 391 (2017) 432–439.
[32] J. Yu, S. Wang, B. Cheng, Z. Lin, F. Huang, Noble metal-free Ni(OH)$_2$-g-C_3N_4 composite photocatalyst with enhanced visible-light photocatalytic H_2-production activity, Catal. Sci. Technol. 3 (2013) 1782–1789.
[33] Z. Zhu, X. Tang, C. Ma, M. Song, N. Gao, Y. Wang, P. Huo, Z. Lu, Y. Yan, Fabrication of conductive and high-dispersed Ppy@Ag/g-C_3N_4 composite photocatalysts for removing various pollutants in water, Appl. Surf. Sci. 387 (2016) 366–374.
[34] J. Yu, K. Wang, W. Xiao, B. Cheng, Photocatalytic reduction of CO_2 into hydrocarbon solar fuels over g-C_3N_4-Pt nanocomposite photocatalysts, Phys. Chem. Chem. Phys. 16 (2014) 11492–11501.
[35] J. Lei, Y. Chen, L. Wang, Y. Liu, J. Zhang, Highly condensed g-C_3N_4-modified TiO_2 catalysts with enhanced photodegradation performance toward acid orange 7, J. Mater. Sci. 50 (2015) 3467–3476.
[36] Z. Zhang, Y. Zhang, L. Lu, Y. Si, S. Zhang, Y. Chen, K. Dai, P. Duan, L. Duan, J. Liu, Graphitic carbon nitride nanosheet for photocatalytic hydrogen production: the impact of morphology and element composition, Appl. Surf. Sci. 391 (2017) 369–375.
[37] D. Chen, J. Yang, H. Ding, Synthesis of nanoporous carbon nitride using calcium carbonate as templates with enhanced visible-light photocatalytic activity, Appl. Surf. Sci. 391 (2017) 384–391.
[38] H. Zuo, C. Lu, Y. Ren, Y. Li, Y. Zhang, W. Chen, Pt_4 clusters supported on monolayer graphitic carbon nitride sheets for oxygen adsorption: a first-principles study, Acta Phys.—Chim. Sin. 32 (2016) 1183–1190.
[39] X. Zhang, M. Zhao, A. Wang, X. Wang, A. Du, Spin-polarization and ferromagnetism of graphitic carbon nitride materials, J. Mater. Chem. C 1 (2013)

6265–6270.
[40] B. Zhu, J. Zhang, C. Jiang, B. Cheng, J. Yu, First principle investigation of halogen-doped monolayer g-C_3N_4 photocatalyst, Appl. Catal. B: Environ. 207 (2017) 27–34.
[41] T. Tong, B. Zhu, C. Jiang, B. Cheng, J. Yu, Mechanistic insight into the enhanced photocatalytic activity of single-atom Pt, Pd or Au-embedded g-C_3N_4, Appl. Surf. Sci. 433 (2018) 1175–1183.
[42] X. Ma, Y. Lv, J. Xu, Y. Liu, R. Zhang, Y. Zhu, A strategy of enhancing the photoactivity of g-C_3N_4 via doping of nonmetal elements: a first-principles study, J. Phys. Chem. C 116 (2012) 23485–23493.
[43] B. Zhu, P. Xia, Y. Li, W. Ho, J. Yu, Fabrication and photocatalytic activity enhanced mechanism of direct Z-scheme g-C_3N_4/Ag_2WO_4 photocatalyst, Appl. Surf. Sci. 391 (2017) 175–183.
[44] H. Li, L. Zhou, L. Wang, Y. Liu, J. Lei, J. Zhang, In situ growth of TiO_2 nanocrystals on g-C_3N_4 for enhanced photocatalytic performance, Phys. Chem. Chem. Phys. 17 (2015) 17406–17412.
[45] Q. He, F. Zhou, S. Zhan, Y. Yang, Y. Liu, Y. Tian, N. Huang, Enhancement of photocatalytic and photoelectrocatalytic activity of Ag modified Mpg-C_3N_4 composites, Appl. Surf. Sci. 391 (2017) 423–431.
[46] J. Zhang, P. Zhou, J. Liu, J. Yu, New understanding of the difference of photocatalytic activity among anatase, rutile and brookite TiO_2, Phys. Chem. Chem. Phys. 16 (2014) 20382–20386.
[47] W. Yu, J. Zhang, T. Peng, New insight into the enhanced photocatalytic activity of N-, C- and S-doped ZnO photocatalysts, Appl. Catal. B: Environ. 181 (2016) 220–227.
[48] M. Dong, P. Zhou, C. Jiang, B. Cheng, J. Yu, First-principles investigation of Cu-doped ZnS with enhanced photocatalytic hydrogen production activity, Chem. Phys. Lett. 668 (2017) 1–6.
[49] J. Zhang, S. Wageh, A. Al-Ghamdi, J. Yu, New understanding on the different photocatalytic activity of wurtzite and zinc-blende CdS, Appl. Catal. B: Environ. 192 (2016) 101–107.
[50] J. Fu, B. Zhu, W. You, M. Jaroniec, J. Yu, A flexible bio-inspired H_2-production photocatalyst, Appl. Catal. B: Environ. 220 (2018) 148–160.
[51] J. Cui, S. Liang, X. Wang, J. Zhang, First principle modeling of oxygen-doped monolayer graphitic carbon nitride, Mater. Chem. Phys. 161 (2015) 194–200.
[52] L. Ruan, G. Xu, L. Gu, C. Li, Y. Zhu, Y. Lu, The physical properties of Li-doped g-C_3N_4 monolayer sheet investigated by the first-principles, Mater. Res. Bull. 66 (2015) 156–162.
[53] J. Liu, B. Cheng, J. Yu, A new understanding of the photocatalytic mechanism of the direct Z-scheme g-C_3N_4/TiO_2 heterostructure, Phys. Chem. Chem. Phys. 18 (2016) 31175–31183.
[54] H. Zhang, Y.F. Zhu, M. Zhao, Interface charge transfer and enhanced visible light response of graphene/anatase TiO_2 (110) systems with and without oxygen vacancy: a DFT + U calculation, Appl. Surf. Sci. 420 (2017) 105–109.
[55] L. Zhu, X. Ma, N. Liu, G. Xu, C. Huang, Band structure modulation and carrier transport process of g-C_3N_4 doped with alkali metals, Acta Phys.—Chim. Sin. 32 (2016) 2488–2494.
[56] T. Di, B. Zhu, B. Cheng, J. Yu, J. Xu, A direct Z-scheme g-C_3N_4/SnS_2 photocatalyst with superior visible-light CO_2 reduction performance, J. Catal. 352 (2017) 532–541.
[57] K. Ding, L. Wen, M. Huang, Y. Zhang, Y. Lu, Z. Chen, How does the B,F-mono-doping and B/F-codoping affect the photocatalytic water-splitting performance of g-C_3N_4? Phys. Chem. Chem. Phys. 18 (2016) 19217–19226.
[58] J. Zhang, F. Ren, M. Deng, Y. Wang, Enhanced visible-light photocatalytic activity of a g-C_3N_4/$BiVO_4$ nanocomposite: a first-principles study, Phys. Chem. Chem. Phys. 17 (2015) 10218–10226.
[59] L. Sun, Y. Qi, C.J. Jia, Z. Jin, W. Fan, Enhanced visible-light photocatalytic activity of g-C_3N_4/Zn_2GeO_4 heterojunctions with effective interfaces based on band match, Nanoscale 6 (2014) 2649–2659.
[60] J. Liu, Effect of phosphorus doping on electronic structure and photocatalytic performance of g-C_3N_4: insights from hybrid density functional calculation, J. Alloys Compd. 672 (2016) 271–276.
[61] S. Wei, F. Wang, M. Dan, K. Zeng, Y. Zhou, The role of high oxygen vacancy concentration on modification of surface properties and H_2S adsorption on the rutile TiO_2 (110), Appl. Surf. Sci. 422 (2017) 990–996.
[62] S. Lu, C. Li, H.H. Li, Y.F. Zhao, Y.Y. Gong, L.Y. Niu, X.J. Liu, T. Wang, The effects of nonmetal dopants on the electronic, optical and chemical performances of monolayer g-C_3N_4 by first-principles study, Appl. Surf. Sci. 392 (2017) 966–974.
[63] J. Xu, G. Wang, J. Fan, B. Liu, S. Cao, J. Yu, g-C_3N_4 modified TiO_2 nanosheets with enhanced photoelectric conversion efficiency in dye-sensitized solar cells, J. Power Sources 274 (2015) 77–84.
[64] Q. Hao, S. Hao, X. Niu, X. Li, D. Chen, H. Ding, Enhanced photochemical oxidation ability of carbon nitride by π-π stacking interactions with graphene, Chin. J. Catal. 38 (2017) 278–286.
[65] L. Ruan, Y. Zhu, L. Qiu, Y. Yuan, Y. Lu, First principles calculations of the pressure affection to g-C_3N_4, Comput. Mater. Sci. 91 (2014) 258–265.
[66] B. Zhu, P. Xia, W. Ho, J. Yu, Isoelectric point and adsorption activity of porous g-C_3N_4, Appl. Surf. Sci. 344 (2015) 188–195.
[67] F. Dong, Y. Sun, L. Wu, M. Fu, Z. Wu, Facile transformation of low cost thiourea into nitrogen-rich graphitic carbon nitride nanocatalyst with high visible light photocatalytic performance, Catal. Sci. Technol. 2 (2012) 1332–1335.
[68] Y. Zhang, J. Liu, G. Wu, W. Chen, Porous graphitic carbon nitride synthesized via direct polymerization of urea for efficient sunlight-driven photocatalytic hydrogen production, Nanoscale 4 (2012) 5300–5303.
[69] J. Mao, T. Peng, X. Zhang, K. Li, L. Ye, L. Zan, Effect of graphitic carbon nitride microstructures on the activity and selectivity of photocatalytic CO_2 reduction under visible light, Catal. Sci. Technol. 3 (2013) 1253–1260.
[70] W. Zhang, Z. Zhao, F. Dong, Y. Zhang, Solvent-assisted synthesis of porous g-C_3N_4 with efficient visible-light photocatalytic performance for NO removal, Chin. J. Catal. 38 (2017) 372–378.
[71] W. Iqbal, C. Dong, M. Xing, X. Tan, J. Zhang, Eco-friendly one-pot synthesis of well-adorned mesoporous g-C_3N_4 with efficiently enhanced visible light photocatalytic activity, Catal. Sci. Technol. 7 (2017) 1726–1734.
[72] W. Iqbal, L. Wang, X. Tan, J. Zhang, One-step in situ green template mediated porous graphitic carbon nitride for efficient visible light photocatalytic activity, J. Environ. Chem. Eng. 5 (2017) 3500–3507.
[73] A. Shi, H. Li, S. Yin, B. Liu, J. Zhang, Y. Wang, Effect of conjugation degree and delocalized π-system on the photocatalytic activity of single layer g-C_3N_4, Appl. Catal. B: Environ. 218 (2017) 137–146.
[74] S. Li, Z. Wang, X. Wang, F. Sun, K. Gao, N. Hao, Z. Zhang, Z. Ma, H. Li, X. Huang, W. Huang, Orientation controlled preparation of nanoporous carbon nitride fibers and related composite for gas sensing under ambient conditions, Nano Res. 10 (2017) 1710–1719.
[75] J. Liu, G. Cao, Z. Yang, D. Wang, D. Dubois, X. Zhou, G.L. Graff, L.R. Pederson, J. Zhang, Oriented nanostructures for energy conversion and storage, ChemSusChem 1 (2008) 676–697.
[76] X. Zhang, H. Wang, H. Wang, Q. Zhang, J. Xie, Y. Tian, J. Wang, Y. Xie, Single-layered graphitic-C_3N_4 quantum dots for two-photon fluorescence imaging of cellular nucleus, Adv. Mater. 26 (2014) 4438–4443.
[77] B. Sun, N. Lu, Y. Su, H. Yu, X. Meng, Z. Gao, Decoration of TiO_2 nanotube arrays by graphitic-C_3N_4 quantum dots with improved photoelectrocatalytic performance, Appl. Surf. Sci. 394 (2017) 479–487.
[78] Y. Su, B. Sun, S. Chen, H. Yu, J. Liu, Fabrication of graphitic-C_3N_4 quantum dots coated silicon nanowire array as a photoelectrode for vigorous degradation of 4-chlorophenol, RSC Adv. 7 (2017) 14832–14836.
[79] Y. Zhao, F. Zhao, X. Wang, C. Xu, Z. Zhang, G. Shi, L. Qu, Graphitic carbon nitride nanoribbons: graphene-assisted formation and synergic function for highly efficient hydrogen evolution, Angew. Chem. Int. Ed. 53 (2014) 13934–13939.
[80] M. Tahir, C. Cao, N. Mahmood, F.K. Butt, A. Mahmood, F. Idrees, S. Hussain, M. Tanveer, Z. Ali, I. Aslam, Multifunctional g-C_3N_4 nanofibers: a template-free fabrication and enhanced optical, electrochemical, and photocatalyst properties, ACS Appl. Mater. Interfaces 6 (2014) 1258–1265.
[81] S. Wang, C. Li, T. Wang, P. Zhang, A. Li, J. Gong, Controllable synthesis of nanotube-type graphitic C_3N_4 and their visible-light photocatalytic and fluorescent properties, J. Mater. Chem. A 2 (2014) 2885–2890.
[82] Y. Wang, H. Wang, F. Chen, F. Cao, X. Zhao, S. Meng, Y. Cui, Facile synthesis of oxygen doped carbon nitride hollow microsphere for photocatalysis, Appl. Catal. B: Environ. 206 (2017) 417–425.
[83] J. Sun, J. Zhang, M. Zhang, M. Antonietti, X. Fu, X. Wang, Bioinspired hollow semiconductor nanospheres as photosynthetic nanoparticles, Nat. Commun. (2012) 1139.
[84] L. Feng, Y. Zou, C. Li, S. Gao, L. Zhou, Q. Sun, M. Fan, H. Wang, D. Wang, G. Li, X. Zou, Nanoporous sulfur-doped graphitic carbon nitride microrods: a durable catalyst for visible-light-driven H_2 evolution, Int. J. Hydrogen Energy 39 (2014) 15373–15379.
[85] Z. You, Y. Su, Y. Yu, H. Wang, T. Qin, F. Zhang, Q. Shen, H. Yang, Preparation of g-C_3N_4 nanorod/$InVO_4$ hollow sphere composite with enhanced visible-light photocatalytic activities, Appl. Catal. B: Environ. 213 (2017) 127–135.
[86] B. Tahir, M. Tahir, N.A.S. Amin, Photo-induced CO_2 reduction by CH_4/H_2O to fuels over Cu-modified g-C_3N_4 nanorods under simulated solar energy, Appl. Surf. Sci. 419 (2017) 875–885.
[87] M. Tahir, C. Cao, F.K. Butt, S. Butt, F. Idrees, Z. Ali, I. Aslam, M. Tanveer, A. Mahmood, N. Mahmood, Large scale production of novel g-C_3N_4 micro strings with high surface area and versatile photodegradation ability, CrystEngComm 16 (2014) 1825–1830.
[88] S. Zhai, P. Guo, J. Zheng, P. Zhao, B. Suo, Y. Wan, First principle study of electronic structures and optical absorption properties of O and S doped graphite phase carbon nitride $(g\text{-}C_3N_4)_6$ quantum dots, Acta Phys. Sin. 66 (2017) 187102.
[89] J. Gracia, P. Kroll, First principles study of C_3N_4 carbon nitride nanotubes, J. Mater. Chem. 19 (2009) 3020–3026.
[90] H. Pan, Y. Zhang, V.B. Shenoy, H. Gao, Ab initio study on a novel photocatalyst: functionalized graphitic carbon nitride nanotube, ACS Catal. 1 (2011) 99–104.
[91] Q. Gao, S. Hu, Y. Du, Z. Hu, The origin of the enhanced photocatalytic activity of carbon nitride nanotubes: a first-principles study, J. Mater. Chem. A 5 (2017) 4827–4834.
[92] J. Liu, B. Cheng, New understanding of photocatalytic properties of zigzag and armchair g-C_3N_4 nanotubes from electronic structures and carrier effective mass, Appl. Surf. Sci. (2017), http://dx.doi.org/10.1016/j.apsusc.2017.06.205.
[93] J. Wen, J. Xie, X. Chen, X. Li, A review on g-C_3N_4-based photocatalysts, Appl. Surf. Sci. 391 (2017) 72–123.
[94] B. Chai, J. Yan, C. Wang, Z. Ren, Y. Zhu, Enhanced visible light photocatalytic degradation of Rhodamine B over phosphorus doped graphitic carbon nitride, Appl. Surf. Sci. 391 (2017) 376–383.
[95] Z. Huang, J. Song, L. Pan, Z. Wang, X. Zhang, J. Zou, W. Mi, X. Zhang, L. Wang, Carbon nitride with simultaneous porous network and O-doping for efficient solar-energy-driven hydrogen evolution, Nano Energy 12 (2015) 646–656.
[96] J. Fu, B. Zhu, C. Jiang, B. Cheng, W. You, J. Yu, Hierarchical porous O-doped g-C_3N_4 with enhanced photocatalytic CO_2 reduction activity, Small 13 (2017) 1603938.
[97] G. Liu, P. Niu, C. Sun, S.C. Smith, Z. Chen, G. Lu, H. Cheng, Unique electronic structure induced high photoreactivity of sulfur-doped graphitic C_3N_4, J. Am. Chem. Soc. 132 (2010) 11642–11648.

[98] Q. Zheng, D.P. Durkin, J.E. Elenewski, Y. Sun, N.A. Banek, L. Hua, H. Chen, M.J. Wagner, W. Zhang, D. Shuai, Visible-light-responsive graphitic carbon nitride: rational design and photocatalytic applications for water treatment, Environ. Sci. Technol. 50 (2016) 12938–12948.

[99] S. Lin, X. Ye, X. Gao, J. Huang, Mechanistic insight into the water photooxidation on pure and sulfur-doped g-C_3N_4 photocatalysts from DFT calculations with dispersion corrections, J. Mol. Catal. A: Chem. 406 (2015) 137–144.

[100] Y. Guo, T. Chen, Q. Liu, Z. Zhang, X. Fang, Insight into the enhanced photocatalytic activity of potassium and iodine codoped graphitic carbon nitride photocatalysts, J. Phys. Chem. C 120 (2016) 25328–25337.

[101] P. Qiu, C. Xu, H. Chen, F. Jiang, X. Wang, R. Lu, X. Zhang, One step synthesis of oxygen doped porous graphitic carbon nitride with remarkable improvement of photo-oxidation activity: role of oxygen on visible light photocatalytic activity, Appl. Catal. B: Environ. 206 (2017) 319–327.

[102] S. Cao, Q. Huang, B. Zhu, J. Yu, Trace-level phosphorus and sodium co-doping of g-C_3N_4 for enhanced photocatalytic H_2 production, J. Power Sources 351 (2017) 151–159.

[103] Y. Wang, Y. Di, M. Antonietti, H. Li, X. Chen, X. Wang, Excellent visible-light photocatalysis of fluorinated polymeric carbon nitride solids, Chem. Mater. 22 (2010) 5119–5121.

[104] X. Wu, S. Jiang, S. Song, C. Sun, Constructing effective photocatalytic purification system with P-introduced g-C_3N_4 for elimination of UO_2^{2+}, Appl. Surf. Sci. (2017), http://dx.doi.org/10.1016/j.apsusc.2017.06.065.

[105] Q. Guo, Y. Zhang, J. Qiu, G. Dong, Engineering the electronic structure and optical properties of g-C_3N_4 by non-metal ion doping, J. Mater. Chem. C 4 (2016) 6839–6847.

[106] C. Lu, P. Zhang, S. Jiang, X. Wu, S. Song, M. Zhu, Z. Lou, Z. Li, F. Liu, Y. Liu, Y. Wang, Z. Le, Photocatalytic reduction elimination of UO_2^{2+} pollutant under visible light with metal-free sulfur doped g-C_3N_4 photocatalyst, Appl. Catal. B: Environ. 200 (2017) 378–385.

[107] L. Ke, P. Li, X. Wu, S. Jiang, M. Luo, Y. Liu, Z. Le, C. Sun, S. Song, Graphene-like sulfur-doped g-C_3N_4 for photocatalytic reduction elimination of UO_2^{2+} under visible Light, Appl. Catal. B: Environ. 205 (2017) 319–326.

[108] C. Liu, Y. Zhang, F. Dong, A.H. Reshak, L. Ye, N. Pinna, C. Zeng, T. Zhang, H. Huang, Chlorine intercalation in graphitic carbon nitride for efficient photocatalysis, Appl. Catal. B: Environ. 203 (2017) 465–474.

[109] J. Ran, T.Y. Ma, G. Gao, X. Du, S.Z. Qiao, Porous P-doped graphitic carbon nitride nanosheets for synergistically enhanced visible-light photocatalytic H_2 production, Energy Environ. Sci. 8 (2015) 3708–3717.

[110] G. Gao, Y. Jiao, E.R. Waclawik, A. Du, Single atom (Pd/Pt) supported on graphitic carbon nitride as an efficient photocatalyst for visible-light reduction of carbon dioxide, J. Am. Chem. Soc. 138 (2016) 6292–6297.

[111] Y.Z. Abdullahi, T.L. Yoon, M.M. Halim, M.R. Hashim, M.Z. Mat Jafri, L.T. Leng, Geometric and electric properties of graphitic carbon nitride sheet with embedded single manganese atom under bi-axial tensile strain, Curr. Appl. Phys. 16 (2016) 809–815.

[112] D. Ghosh, G. Periyasamy, B. Pandey, S.K. Pati, Computational studies on magnetism and the optical properties of transition metal embedded graphitic carbon nitride sheets, J. Mater. Chem. C 2 (2014) 7943–7951.

[113] Z. Sun, J.M.T.A. Fischer, Q. Li, J. Hu, Q. Tang, H. Wang, Z. Wu, M. Hankel, D.J. Searles, L. Wang, Enhanced CO_2 photocatalytic reduction on alkali-decorated graphitic carbon nitride, Appl. Catal. B: Environ. 216 (2017) 146–155.

[114] Y. Zou, X. Wang, Y. Ai, Y. Liu, Y. Ji, H. Wang, T. Hayat, A. Alsaedi, W. Hu, X. Wang, β-Cyclodextrin modified graphitic carbon nitride for the removal of pollutants from aqueous solution: experimental and theoretical calculation study, J. Mater. Chem. A 4 (2016) 14170–14179.

[115] S. Hu, X. Chen, Q. Li, F. Li, Z. Fan, H. Wang, Y. Wang, B. Zheng, G. Wu, Fe^{3+} doping promoted N_2 photofixation ability of honeycombed graphitic carbon nitride: the experimental and density functional theory simulation analysis, Appl. Catal. B: Environ. 201 (2017) 58–69.

[116] T. Xiong, W. Cen, Y. Zhang, F. Dong, Bridging the g-C_3N_4 interlayers for enhanced photocatalysis, ACS Catal. 6 (2016) 2462–2472.

[117] G. Li, L. Li, H. Yuan, H. Wang, H. Zeng, J. Shi, Alkali-assisted mild aqueous exfoliation for single-layered and structure-preserved graphitic carbon nitride nanosheets, J. Colloid Interface Sci. 495 (2017) 19–26.

[118] J. Zhang, Y. Wang, J. Jin, J. Zhang, Z. Lin, F. Huang, J. Yu, Efficient visible-light photocatalytic hydrogen evolution and enhanced photostability of core/shell CdS/g-C_3N_4 nanowires, ACS Appl. Mater. Interfaces 5 (2013) 10317–10324.

[119] F. Chen, H. Yang, X. Wang, H. Yu, Facile synthesis and enhanced photocatalytic H_2-evolution performance of NiS_2-modified g-C_3N_4 photocatalysts, Chin. J. Catal. 38 (2017) 296–304.

[120] W. Zhang, X. Xiao, Y. Li, X. Zeng, L. Zheng, C. Wan, Liquid-exfoliation of layered MoS_2 for enhancing photocatalytic activity of TiO_2/g-C_3N_4 photocatalyst and DFT study, Appl. Surf. Sci. 389 (2016) 496–506.

[121] W. Yu, D. Xu, T. Peng, Enhanced photocatalytic activity of g-C_3N_4 for selective CO_2 reduction to CH_3OH via facile coupling of ZnO: a direct Z-scheme mechanism, J. Mater. Chem. A 3 (2015) 19936–19947.

[122] J. Yu, S. Wang, J. Low, W. Xiao, Enhanced photocatalytic performance of direct Z-scheme g-C_3N_4-TiO_2 photocatalysts for the decomposition of formaldehyde in air, Phys. Chem. Chem. Phys. 15 (2013) 16883–16890.

[123] L. Zhou, L. Wang, J. Zhang, J. Lei, Y. Liu, The preparation, and applications of g-C_3N_4/TiO_2 heterojunction catalysts—a review, Res. Chem. Intermed. 43 (2016) 2081–2101.

[124] K. He, J. Xie, X. Luo, J. Wen, S. Ma, X. Li, Y. Fang, X. Zhang, Enhanced visible light photocatalytic H_2 production over Z-scheme g-C_3N_4 nansheets/WO_3 nanorods nanocomposites loaded with $Ni(OH)_x$ cocatalysts, Chin. J. Catal. 38 (2017) 240–252.

[125] T. Ohno, N. Murakami, T. Koyanagi, Y. Yang, Photocatalytic reduction of CO_2 over a hybrid photocatalyst composed of WO_3 and graphitic carbon nitride (g-C_3N_4) under visible light, J. CO_2 Util. 6 (2014) 17–25.

[126] S. Shi, M.A. Gondal, S.G. Rashid, Q. Qi, A.A. Al-Saadi, Z.H. Yamani, Y. Sui, Q. Xu, K. Shen, Synthesis of g-C_3N_4/$BiOCl_xBr_{1-x}$ hybrid photocatalysts and the photoactivity enhancement driven by visible light, Colloids Surf. A: Physicochem. Eng. Asp. 461 (2014) 202–211.

[127] S. Zhan, F. Zhou, N. Huang, Y. Yang, Y. Liu, Y. Yin, Y. Fang, g-C_3N_4/$ZnWO_4$ films: preparation and its enhanced photocatalytic decomposition of phenol in UV, Appl. Surf. Sci. 358 (2015) 328–335.

[128] L. Sun, X. Zhao, C. Jia, Y. Zhou, X. Cheng, P. Li, L. Liu, W. Fan, Enhanced visible-light photocatalytic activity of g-C_3N_4-$ZnWO_4$ by fabricating a heterojunction: investigation based on experimental and theoretical studies, J. Mater. Chem. 22 (2012) 23428–28438.

[129] H. Sun, J. Li, G. Zhang, N. Li, Microtetrahedronal $Bi_{12}TiO_{20}$/g-C_3N_4 composite with enhanced visible light photocatalytic activity toward gaseous formaldehyde degradation: facet coupling effect and mechanism study, J. Mol. Catal. A: Chem. 424 (2016) 311–322.

[130] Y. Jiang, P. Liu, Y. Chen, Z. Zhou, H. Yang, Y. Hong, F. Li, L. Ni, Y. Yan, D.H. Gregory, Construction of stable Ta_3N_5/g-C_3N_4 metal/non-metal nitride hybrids with enhanced visible-light photocatalysis, Appl. Surf. Sci. 391 (2017) 392–403.

[131] B. Wang, J. Zhang, F. Huang, Enhanced visible light photocatalytic H_2 evolution of metal-free g-C_3N_4/SiC heterostructured photocatalysts, Appl. Surf. Sci. 391 (2017) 449–456.

[132] J. Luo, X. Zhou, L. Ma, X. Xu, Rational construction of Z-scheme Ag_2CrO_4/g-C_3N_4 composites with enhanced visible-light photocatalytic activity, Appl. Surf. Sci. 390 (2016) 357–367.

[133] S. Cao, J. Low, J. Yu, M. Jaroniec, Polymeric photocatalysts based on graphitic carbon nitride, Adv. Mater. 27 (2015) 2150–2176.

[134] J. Low, J. Yu, M. Jaroniec, S. Wageh, A.A. Al-Ghamdi, Heterojunction photocatalysts, Adv. Mater. 29 (2017) 1601694.

[135] J. Fu, J. Yu, C. Jiang, B. Cheng, g-C_3N_4-based heterostructured photocatalysts, Adv. Energy Mater. (2017) 1701503.

[136] J. Low, C. Jiang, B. Cheng, S. Wageh, A.A. Al-Ghamdi, J. Yu, A review of direct Z-scheme photocatalysts, Small Methods 1 (2017) 1700080.

[137] Y. Li, K. Lv, W. Ho, F. Dong, X. Wu, Y. Xia, Hybridization of rutile TiO_2 ($rTiO_2$) with g-C_3N_4 quantum dots (CN QDs): an efficient visible-light-driven Z-scheme hybridized photocatalyst, Appl. Catal. B: Environ. 202 (2017) 611–619.

[138] N. Tian, H. Huang, Y. Guo, Y. He, Y. Zhang, A g-C_3N_4/$Bi_2O_2CO_3$ composite with high visible-light-driven photocatalytic activity for rhodamine B degradation, Appl. Surf. Sci. 322 (2014) 249–254.

[139] J. Lei, F. Liu, L. Wang, Y. Liu, J. Zhang, A binary polymer composite of graphitic carbon nitride and poly(diphenylbutadiyne) with enhanced visible light photocatalytic activity, RSC Adv. 7 (2017) 27377–27383.

[140] J. Wang, Z. Guan, J. Huang, Q. Li, J. Yang, Enhanced photocatalytic mechanism for the hybrid g-C_3N_4/MoS_2 nanocomposite, J. Mater. Chem. A 2 (2014) 7960–7966.

[141] J. Liu, Origin of high photocatalytic efficiency in monolayer g-C_3N_4/CdS heterostructure: a hybrid DFT study, J. Phys. Chem. C 119 (2015) 28417–28423.

[142] J. Li, M. Zhang, Q. Li, J. Yang, Enhanced visible light activity on direct contact Z-scheme g-C_3N_4-TiO_2 photocatalyst, Appl. Surf. Sci. 391 (2017) 184–193.

[143] W. Yu, J. Chen, T. Shang, L. Chen, L. Gu, T. Peng, Direct Z-scheme g-C_3N_4/WO_3 photocatalyst with atomically defined junction for H_2 production, Appl. Catal. B: Environ. 219 (2017) 693–704.

[144] L. Cui, X. Ding, Y. Wang, H. Shi, L. Huang, Y. Zuo, S. Kang, Facile preparation of Z-scheme WO_3/g-C_3N_4 composite photocatalyst with enhanced photocatalytic performance under visible light, Appl. Surf. Sci. 391 (2017) 202–210.

[145] S. Cao, J. Yu, Carbon-based H_2-production photocatalytic materials, J. Photochem. Photobiol. C 27 (2016) 72–99.

[146] X. Li, J. Yu, S. Wageh, A.A. Al-Ghamdi, J. Xie, Graphene in photocatalysis: a review, Small 12 (2016) 6640–6696.

[147] J. Low, J. Yu, W. Ho, Graphene-based photocatalysts for CO_2 reduction to solar fuel, J. Phys. Chem. Lett. 6 (2015) 4244–4251.

[148] Q. Li, X. Li, S. Wageh, A.A. Al-Ghamdi, J. Yu, CdS/graphene nanocomposite photocatalysts, Adv. Energy Mater. 5 (2015) 1500010.

[149] Q. Xu, B. Cheng, J. Yu, G. Liu, Making co-condensed amorphous carbon/g-C_3N_4 composites with improved visible-light photocatalytic H_2-production performance using Pt as cocatalyst, Carbon 118 (2017) 241–249.

[150] Y. Li, Y. Sun, F. Dong, W.K. Ho, Enhancing the photocatalytic activity of bulk g-C_3N_4 by introducing mesoporous structure and hybridizing with graphene, J. Colloid Interface Sci. 436 (2014) 29–36.

[151] G. Liao, S. Chen, X. Quan, H. Yu, H. Zhao, Graphene oxide modified g-C_3N_4 hybrid with enhanced photocatalytic capability under visible light irradiation, J. Mater. Chem. 22 (2012) 2721–2726.

[152] Z. Wu, H. Gao, S. Yan, Z. Zou, Synthesis of carbon black/carbon nitride intercalation compound composite for efficient hydrogen production, Dalton Trans. 43 (2014) 12013–12017.

[153] X. Chen, H. Chen, J. Guan, J. Zhen, Z. Sun, P. Du, Y. Lu, S. Yang, A facile mechanochemical route to a covalently bonded graphitic carbon nitride (g-C_3N_4) and fullerene hybrid toward enhanced visible light photocatalytic hydrogen production, Nanoscale 9 (2017) 5615–5623.

[154] X. Jian, X. Liu, H. Yang, J. Li, X. Song, H. Dai, Z. Liang, Construction of carbon quantum dots/proton-functionalized graphitic carbon nitride nanocomposite via electrostatic self-assembly strategy and its application, Appl. Surf. Sci. 370 (2016)

514–521.
[155] J. Liu, Y. Liu, N. Liu, Y. Han, X. Zhang, H. Huang, Y. Lifshitz, S. Lee, J. Zhong, Z. Kang, Metal-free efficient photocatalyst for stable visible water splitting via a two-electron pathway, Science 347 (2015) 970–974.
[156] A. Du, S. Sanvito, Z. Li, D. Wang, Y. Jiao, T. Liao, Q. Sun, Y.H. Ng, Z. Zhu, R. Amal, S.C. Smith, Hybrid graphene and graphitic carbon nitride nanocomposite: gap opening, electron-hole puddle, interfacial charge transfer, and enhanced visible light response, J. Am. Chem. Soc. 134 (2012) 4393–4397.
[157] G. Gao, Y. Jiao, F. Ma, Y. Jiao, E. Waclawik, A. Du, Carbon nanodot decorated graphitic carbon nitride: new insights into the enhanced photocatalytic water splitting from *ab initio* studies, Phys. Chem. Chem. Phys. 17 (2015) 31140–31144.
[158] Q. Li, L. Xu, K. Luo, W. Huang, L. Wang, X. Li, G. Huang, Y. Yu, Insights into enhanced visible-light photocatalytic activity of C_{60} modified g-C_3N_4 hybrids: the role of nitrogen, Phys. Chem. Chem. Phys. 18 (2016) 33094–33102.
[159] Y. Gong, H. Yu, S. Chen, X. Quan, Constructing metal-free polyimide/g-C_3N_4 with high photocatalytic activity under visible light irradiation, RSC Adv. 5 (2015) 83225–83231.
[160] S. Chu, C. Wang, J. Feng, Y. Wang, Z. Zou, Melem A metal-free unit for photocatalytic hydrogen evolution, Int. J. Hydrogen Energy 39 (2014) 13519–13526.
[161] Z. Chen, P. Sun, B. Fan, Q. Liu, Z. Zhang, X. Fang, Textural and electronic structure engineering of carbon nitride via doping with π-deficient aromatic pyridine ring for improving photocatalytic activity, Appl. Catal. B: Environ. 170–171 (2015) 10–16.
[162] Y. Li, W. Ho, K. Lv, B. Zhu, S.C. Lee, Carbon vacancy-induced enhancement of the visible light-driven photocatalytic oxidation of NO over g-C_3N_4 nanosheets, Appl. Surf. Sci. (2017), http://dx.doi.org/10.1016/j.apsusc.2017.06.054.
[163] Y. Li, K. Lv, W. Ho, Z. Zhao, Y. Huang, Enhanced visible-light photo-oxidation of nitric oxide using bismuth-coupled graphitic carbon nitride composite heterostructures, Chin. J. Catal. 38 (2017) 321–329.
[164] D.J. Martin, K. Qiu, S.A. Shevlin, A.D. Handoko, X. Chen, Z. Guo, J. Tang, Highly efficient photocatalytic H_2 evolution from water using visible light and structure-controlled graphitic carbon nitride, Angew. Chem. Int. Ed. 53 (2014) 9240–9245.
[165] L. Lin, H. Ou, Y. Zhang, X. Wang, Tri-s-triazine-based crystalline graphitic carbon nitrides for highly efficient hydrogen evolution photocatalysis, ACS Catal. 6 (2016) 3921–3931.
[166] K. Wang, Q. Li, B. Liu, B. Cheng, W. Ho, J. Yu, Sulfur-doped g-C_3N_4 with enhanced photocatalytic CO_2-reduction performance, Appl. Catal. B: Environ. 176–177 (2015) 44–52.
[167] S. Cao, Y. Li, B. Zhu, M. Jaroniec, J. Yu, Facet effect of Pd cocatalyst on photocatalytic CO_2 reduction over g-C_3N_4, J. Catal. 349 (2017) 208–217.
[168] H. Tang, S. Chang, G. Tang, W. Liang, AgBr and g-C_3N_4 co-modified Ag_2CO_3 photocatalyst: a novel multi-heterostructured photocatalyst with enhanced photocatalytic activity, Appl. Surf. Sci. 391 (2017) 440–448.
[169] Z. Liang, Q. Wen, X. Wang, F. Zhang, Y. Yu, Chemically stable and reusable nano zero-valent iron/graphite-like carbon nitride nanohybrid for efficient photocatalytic treatment of Cr(VI) and rhodamine B under visible light, Appl. Surf. Sci. 386 (2016) 451–459.
[170] J. Lei, Y. Chen, F. Shen, L. Wang, Y. Liu, J. Zhang, Surface modification of TiO_2 with g-C_3N_4 for enhanced UV and visible photocatalytic activity, J. Alloys Compd. 631 (2015) 328–334.
[171] J. Bai, X. Chen, Z. Xi, X. Wang, Q. Li, S. Hu, Influence of solvothermal post-treatment on photochemical nitrogen conversion to ammonia with g-C_3N_4 catalyst, Acta Phys.—Chim. Sin. 33 (2017) 611–619.
[172] H. Ma, Z. Shi, Q. Li, S. Li, Preparation of graphitic carbon nitride with large specific surface area and outstanding N_2 photofixation ability via a dissolve-regrowth process, J. Phys. Chem. Solids 99 (2016) 51–58.
[173] S.M. Aspera, M. David, H. Kasai, First-principles study of the adsorption of water on tri-s-triazine-based graphitic carbon nitride, Jpn. J. Appl. Phys. 49 (2010) 115703.
[174] S.M. Aspera, H. Kasai, H. Kawai, Density functional theory-based analysis on O_2 molecular interaction with the tri-s-triazine-based graphitic carbon nitride, Surf. Sci. 606 (2012) 892–901.
[175] H.Z. Wu, L.M. Liu, S.J. Zhao, The effect of water on the structural, electronic and photocatalytic properties of graphitic carbon nitride, Phys. Chem. Chem. Phys. 16 (2014) 3299–3304.
[176] H. Wu, S. Bandaru, J. Liu, L. Li, Z. Wang, Adsorption of H_2O, H_2, O_2, CO, NO, and CO_2 on graphene/g-C_3N_4 nanocomposite investigated by density functional theory, Appl. Surf. Sci. (2017), http://dx.doi.org/10.1016/j.apsusc.2017.06.073.
[177] H. Wu, L. Liu, S. Zhao, The role of the defect on the adsorption and dissociation of water on graphitic carbon nitride, Appl. Surf. Sci. 358 (2015) 363–369.
[178] B. Zhu, L. Zhang, D. Xu, B. Cheng, J. Yu, Adsorption investigation of CO_2 on g-C_3N_4 surface by DFT calculation, J. CO_2 Util. 21 (2017) 327–335.
[179] Y. Ji, H. Dong, H. Lin, L. Zhang, T. Hou, Y. Li, Heptazine-based graphitic carbon nitride as an effective hydrogen purification membrane, RSC Adv. 6 (2016) 52377–52383.
[180] P. Xia, B. Zhu, J. Yu, S. Cao, M. Jaroniec, Ultra-thin nanosheet assemblies of graphitic carbon nitride for enhanced photocatalytic CO_2 reduction, J. Mater. Chem. A 5 (2017) 3230–3238.
[181] J. Wirth, R. Neumann, M. Antonietti, P. Saalfrank, Adsorption and photocatalytic splitting of water on graphitic carbon nitride: a combined first principles and semiempirical study, Phys. Chem. Chem. Phys. 16 (2014) 15917–15926.
[182] W. Fu, H. He, Z. Zhang, C. Wu, X. Wang, H. Wang, Q. Zeng, L. Sun, X. Wang, J. Zhou, Q. Fu, P. Yu, Z. Shen, C. Jin, B.I. Yakobson, Z. Liu, Strong interfacial coupling of MoS_2/g-C_3N_4 van de Waals solids for highly active water reduction, Nano Energy 27 (2016) 44–50.
[183] L.M. Azofra, D.R. MacFarlane, C. Sun, A DFT study of planar *vs.* corrugated graphene-like carbon nitride (g-C_3N_4) and its role in the catalytic performance of CO_2 conversion, Phys. Chem. Chem. Phys. 18 (2016) 18507–18514.